# Extended tuning of distributed-feedback lasers in a bias-tee circuit via waveform optimization for MHz-rate absorption spectroscopy

Anil Pradeep Nair, Nicolas Q Minesi, Christopher Jelloian, Nicholas M Kuenning, R Mitchell Spearrin

# Extended tuning of distributed-feedback lasers in a bias-tee circuit via waveform optimization for MHz-rate absorption spectroscopy

**Measurement Science and Technology manuscript No.**
(will be inserted by the editor)

# Extended tuning of distributed-feedback lasers in a bias-tee circuit via waveform optimization for MHz-rate absorption spectroscopy

**Anil P. Nair, Nicolas Q. Minesi, Christopher Jelloian, Nicholas M. Kuenning, R. Mitchell Spearrin**

Department of Mechanical and Aerospace Engineering, University of California, Los Angeles (UCLA), Los Angeles, CA 90095, USA

Received: XXXX / Revised version: XXXX

**Abstract** Variations in injection-current waveform are examined using diplexed RF-modulation with continuous-wave distributed-feedback (CW-DFB) lasers, with the aim to maximize the spectral tuning range and signal-to-noise ratio for MHz-rate laser absorption spectroscopy. Utilizing a bias-tee circuit, laser chirp rates are shown to increase by modulating the AC input voltage using square waves instead of sine waves and by scanning the laser below the lasing threshold during the modulation period. The effect of waveform duty cycle and leading-edge ramp rate are further examined. A spectral scan depth on the order of 1 $cm^{-1}$ at a scan frequency of 1 MHz is achieved with a representative CW-DFB quantum cascade laser near 5 µm. Distortion of high-frequency optical signals due to detector bandwidth is also examined, and limitations are noted for applications with narrow spectral features and low-bandwidth detectors. Based on common detection system limitations, an optimization approach is established for a given detection bandwidth and target spectra. A representative optimization is presented for measurements of sub-atmospheric carbon monoxide spectra with a 200-MHz detection system. The methods are then demonstrated to resolve transient gas properties (pressure and temperature) via laser absorption spectroscopy at MHz rates in a detonation tube and shock tube facility. An appendix detailing a first-order model of high-speed distributed feedback laser tuning dynamics is also included to support the experimental observations of this work.

## 1 Introduction

Microsecond time resolution of thermodynamic and thermochemical properties is critical for the assessment of transient physical processes occurring in many dynamic systems. Laser absorption spectroscopy (LAS) [1] at MHz rates has been demonstrated by various methods [2–5], and has proven useful in measuring gas properties in detonation environments [6, 7], planetary-entry shock layers [3, 8], and in the characterization of energetic materials [9]. The MHz scanned-wavelength techniques used in these works should be distinguished from fixed-wavelength laser absorption [10–14], which is limited in measurement rate solely by detector bandwidth. This approach, while fast, is generally not robust to beam steering, particle scattering, and thermal emission, which are pronounced in harsh and dynamic environments. Fixed-wavelength LAS methods also require assumptions about spectral line shapes to be quantitative. Wavelength-scanning or wavelength-modulation LAS techniques, on the other hand, leverage additional spectral information to mitigate these convoluting effects. The benefits of spectral resolution are enhanced at higher measurement rates (100s of kHz to MHz), as the aforementioned effects are effectively frozen across the measurement period, allowing for more facile correction due to frequency separation. Moreover, extended spectral tuning or sweeping can enable the resolution of multiple spectral lines from which multiple gas properties can be inferred, and potential application at higher pressures where spectral transitions are broadened.

Continuous-wave distributed feedback lasers (CW-DFBs) are highly stable, narrow-linewidth semiconductor light sources with convenient injection-current tunability. CW-DFB lasers have been used extensively in wavelength -scanning or -modulation techniques for gas-phase absorption spectroscopy [15], with low scan-to-scan output variation/noise relative to pulsed operation. Over the past two decades, CW-DFB lasers have been developed throughout the mid-wave infrared, via quantum cascade or interband cascade architectures, providing access to the strongest vibrational absorption bands of most molecules, and thus enabling gas detection of many species at relatively short optical pathlengths, which has attracted new applications. Unfortunately, for CW-DFB lasers, there is an intrinsic trade-off in scan rate and scan spectral range, termed the spectral scan depth $\Delta\nu$ [$cm^{-1}$]. Traditionally, the rate-limiting component in CW-DFB

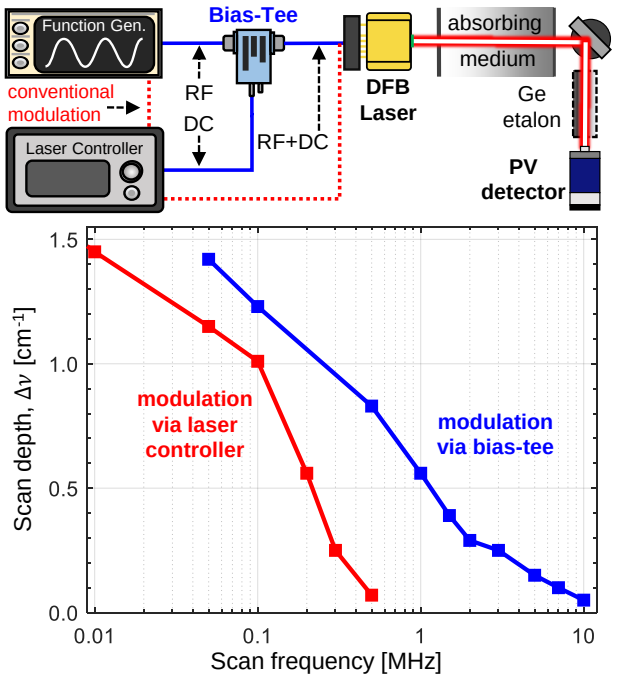


**Fig. 1** *Top left*: Schematic of DFB laser-control setup with conventional modulation in red and RF-modulation hardware with bias-tee in blue. *Top right*: Optical setup for typical laser absorption measurement. *Bottom*: Scan depth *versus* scan frequency with and without bias-tee circuit for quantum cascade laser used in [7].

modulation schemes is the laser-controller bandwidth, which attenuates the external modulation signal before it reaches the laser. This has typically limited CW-DFB laser absorption measurements to rates of 10s to 100s of kHz, which is insufficient to resolve physical phenomena occurring at microsecond timescales. The rapid drop in scan depth with scan rate is indicated by the red curve in Fig. 1 for a CW-DFB QCL for which the current modulation was mediated by an Arroyo 6310-QCL controller [16].

The bandwidth limitation of the laser controller can be bypassed by directly diplexing the current modulation with the steady DC output from the controller with a bias-tee (see Fig. 1). Bias-tee circuits coupled with CW-DFB lasers have been shown to enable a significant improvement in the achievable spectral scan depth at a given scan frequency, particularly near and above 1 MHz. This is highlighted by the blue curve in Fig. 1, which also shows an order of magnitude increase in the effective scan frequency at which 0.1 $cm^{-1}$ of scan depth can be achieved. Our group has recently demonstrated the use of this technique to measure gas properties in detonation engines and shock tubes at rates from 1–3 MHz [7, 8, 17, 18]. The scan depth achievable in our previous work was on the order of 0.5 $cm^{-1}$ at 1 MHz (equivalent to $\Delta\lambda = 1.25$ nm at 5 µm) [7]. While useful, it remains desirable to increase the tuning range or scan depth to collect additional spectral information at such high measurement rates.

In addition to spectral scan depth, the quality of LAS measurement data during a scan period depends heavily on the optical signal-to-noise ratio (SNR)[1] of the detected light intensity, and this depends, in part, on the scan or modulation waveform. Given the coupling of injection-current modulation waveform with CW-DFB laser output intensity, typical modulation waveforms (e.g. sinusoidal, sawtooth) involve periods of high and low output intensity and correspondingly high and low optical SNR. In many cases, large regions of the scan period are not usable due to low optical SNR, and this can be pronounced when maximizing the scan depth and thus scanning near the lasing threshold. As such, in addition to the scan depth extension, there is a further need to improve and maximize the optical SNR of scanned-wavelength CW-DFB laser absorption measurements to increase the quantity and quality of spectral information collected at MHz rates.

In this work, we explore variations of modulation waveform to maximize spectral scan depth and optical SNR for a continuous-wave distributed feedback quantum cascade laser (QCL) in a bias-tee circuit with application to MHz-rate laser absorption spectroscopy. We first describe the optical configuration and methods for characterizing DFB laser tuning dynamics in the context of laser absorption spectroscopy. Subsequent waveform exploration shows significant gains to be made using square-waveform modulation and modulating below the lasing threshold. The high laser chirp rates produced by these waveforms also reveal limitations associated with the detection system bandwidth for measurement of narrow spectra. To compromise these issues, we outline a waveform-optimization strategy to generate a waveform that maximizes laser spectral scan depth and optical SNR without exceeding typical detector bandwidth constraints. This study shows that the combination of the bias-tee circuit and injection-current waveform optimization yields more than an order of magnitude gain in temporal frequency (and effective measurement rate) for a target spectral tuning depth relative to conventional laser modulation. The aforementioned methods are demonstrated for laser absorption sensing in dynamic high-temperature environments (detonation and shock tubes) for MHz-rate measurements of gas pressure and temperature. In the appendix, a first-order model is developed for high-speed distributed feedback laser wave-

[1] The optical SNR of a laser signal is defined here as the ratio of the mean value of a laser signal divided by the standard deviation of the signal due to noise. This "optical" SNR is proportional to the SNR of the end LAS measurement of quantities such as temperature, pressure, or species concentrations (termed "measurement SNR"), but is not not necessarily equal to it, with the relationship between the two influenced by other factors such as absorption strength, temperature sensitivity, and fitting method.

length tuning dynamics and provides physical explanations for the experimental trends noted in this work.

## 2 Methods

This work explores the characteristic tunability of continuous-wave distributed feedback lasers in the infrared with single-mode monochromatic light output. Distributed-feedback lasers consist of a periodic grating structure embedded in the laser gain medium, which acts a distributed Bragg reflector (DBR) [19] that selectively provides optical feedback to a narrow band of wavelengths ($10^{-4}$–$10^{-3}$ $cm^{-1}$ linewidth [20]) related to the spatial periodicity of the grating, enabling stable, single-mode operation. DFB lasers are wavelength-tuned by changing the temperature of the DBR grating, which has the effect of changing its spatial periodicity, which shifts the laser output wavelength [21]. The temperature of the laser can be set using Peltier thermoelectric cooling (TEC) supplied by the laser controller. The temperature of the laser chip can be further increased via resistive heating from the laser injection current, which shifts the laser output wavelength higher than the TEC alone. The laser temperature can be rapidly modulated by injection-current modulation, enabling fast wavelength tuning around the center wavelength set by the TEC and average resistive heating. The relationship between laser temperature and output wavelength and the resulting tuning dynamics are discussed in more detail in the appendix.

In this work, a continuous-wave DFB-QCL (ALPES Lasers), tunable from 2002 to 2012 $cm^{-1}$ was used as the representative light source for scan-depth maximization in a bias-tee circuit. This wavelength was selected due in part to demonstrated utility for LAS measurements of spectral transitions in the fundamental band of carbon monoxide for numerous sensing applications [7, 8, 22–24]. Note that this *continuous-wave* laser must be differentiated from *pulsed* DFB lasers used in other high-speed sensing techniques [25–32], and typically offers better scan-to-scan repeatability in output intensity. The laser temperature and mean injection current are set using an Arroyo 6310-QCL controller. A radio frequency (RF) signal is supplied by a digital function generator (Rigol DG1032Z) which can supply a maximum output frequency of 30 MHz. The function generator can output various waveforms: sine waves, square waves, as well as user-defined arbitrary waveforms. The DC current from the laser driver and the RF current from the function generator are diplexed using a bias-tee circuit to create a modulating injection-current waveform going into the laser. The bias-tee circuitry used to operate the laser is shown at the top left of Fig. 1 and a representative sinusoidal waveform is pictured at the top left of Fig. 2.

A coupled optical detection system was configured to assess the laser tuning dynamics, including output intensity and wavelength variation in time for a given input waveform. The laser beam is focused onto an AC-coupled MCT photovoltaic detector (Vigo PVI-4TE-6-1x1) with a bandwidth that spans between 10 Hz and 200 MHz. The detector output was sampled at 1.25 GS/s using a Textronix MSO44 oscilloscope with a 200 MHz bandwidth. A typical laser output trace is shown for a sinusoidal injection-current waveform on the left of the middle row of Fig. 2. To additionally assess the wavelength scanning or tuning range of the laser, a 50.8-mm germanium etalon was placed into the beam path. The detector and etalon location in the beam path is shown at the top right of Fig. 1. The effective wavelength-dependent transmissivity due to the internal resonance of the etalon induces an oscillatory signal on the detector as the laser wavelength changes in time. This signal is pictured in the middle row of Fig. 2. The etalon peaks are evenly spaced in the spectral domain by the etalon's free spectral range (FSR) of $\sim$0.025 $cm^{-1}$. By identifying the peak locations, the change in laser wavelength/frequency over time can be assessed. The instantaneous change in wavenumber magnitude over the scan is termed the *chirp*, $C$ [$cm^{-1}$] [33]. The chirp profile for a representative sine wave is plotted in the bottom left of Fig. 2. Two regions of the scan period can be identified by increasing or decreasing intensity, also termed upscan and downscan. In the upscan, the laser wavelength is increasing as the laser chip is being heated by the injection current. In the downscan, the laser chip is being cooled and the wavelength is decreasing. Typically, the output intensity of the laser responds within nanoseconds to the injection current, and the laser temperature lags behind, yielding a corresponding lag in wavelength or wavenumber. This lag is pronounced at MHz scan frequencies, which often leads to the wavelength downscan occurring during the portion of the scan with the lowest or zero output intensity, as seen for the sinusoidal waveform in Fig. 2 (see also Eq. 36). This results in poor optical SNR for the downscan, preventing the collection of meaningful spectral information during this part of the scan.

Given that current modulation via the bias-tee circuit involves bypassing the laser driver, which protects the laser from reverse bias, careful procedural steps must be taken when characterizing the laser tuning. Notably, the function generator outputs a voltage signal whereas the laser output depends on the injected current signal. Thus, a transfer function $H$ [$A \cdot V^{-1}$] between the voltage amplitude from the function generator and the injection-current amplitude to the laser must be established. This was determined by first setting the DC current of the laser to some value $i_{DC}$ [A] above the lasing threshold using the laser driver and then slowly increasing the amplitude of an RF sinusoidal waveform from the function generator. By measuring the laser output intensity and noting when the bottom of the sine wave flattens (zero intensity signal), the minimum injection current is assumed to be reaching the lasing threshold current $i_{th}$. By using the known peak-to-peak voltage amplitude of

the function generator output, $V_{\mathrm{pp}}$ [V], the transfer function, $H$, can be determined:

$$H = \frac{2(i_{\mathrm{DC}} - i_{\mathrm{th}})}{V_{\mathrm{pp}}} \tag{1}$$

For the bias-tee and laser system used in this work, the transfer function was approximately 14 mA/V. Knowledge of the transfer function enables the user to identify the actual minimum and maximum current values being applied to the laser for any given function generator output.

With the transfer function known, bounds on the mean injection current and RF voltage amplitude from the function generator can be prescribed. For arbitrary waveforms, the average value of the RF voltage is not necessarily equal to the "midrange" RF voltage $V_{\mathrm{mid}}$ [V], or the average of the maximum and minimum voltage ($V_{\mathrm{max}}$ and $V_{\mathrm{min}}$). As such, the offset of such waveforms should be adjusted on the function generator such that the cycle-averaged mean value of the output waveform is zero, to prevent unpredictable leakage of a DC (or low frequency) signal across the bias-tee. Failure to do so can cause laser overvoltage or reverse-biasing. Also, the DC current supplied by the laser driver should be set such that the maximum RF+DC current $i_{\mathrm{max}}$ does not exceed the current limit of the laser, $i_{\mathrm{lim}}$. This condition can be met by ensuring the following:

$$i_{\mathrm{DC}} \leq i_{\mathrm{lim}} - HV_{\mathrm{max}} \tag{2}$$

Likewise, to prevent reverse-biasing the laser, the minimum RF+DC injection current must be positive. This is enforced by ensuring the DC current satisfies the following condition:

$$i_{\mathrm{DC}} \geq HV_{\mathrm{min}} \tag{3}$$

The spectral tuning and signal-to-noise ratio objectives of this work are aimed towards laser absorption spectroscopy (LAS). The basics of LAS methods are well-described in prior literature [15, 34], and thus largely omitted here. While the waveform optimization methods are mostly independent of the target absorption features, the effective temporal frequency content of the target absorptivity must be considered. To acquire LAS measurements, a laser beam is directed through an absorbing medium as pictured in Fig. 1. Before the absorbing medium is present, a measurement of the laser raw intensity $I_0$ is taken, known as the "background" signal. Once the absorbing gas is present in the line-of-sight, a second measurement of the transmitted intensity $I_{\mathrm{tr}}$ is taken. The ratio of these signals is used to obtain the spectral absorbance $\alpha_\nu$ using the following relation:

$$\alpha_\nu = -\ln\left(\frac{I_{\mathrm{tr}}}{I_0}\right)_\nu \tag{4}$$

The time-resolved absorbance spectrum can be mapped to the wavenumber domain by using the chirp profile obtained with the etalon signal. This absorbance spectrum can then be analyzed to extract information about the properties of the medium in question, such as gas temperature, pressure, and composition. In Section 3, the relevance of the characteristic temporal frequency associated with changes in $\alpha_\nu$ from wavelength scanning is described in the context of laser tuning dynamics. Demonstrations of LAS measurements at MHz rates are also presented.

## 3 Results and analysis

### *3.1 Laser tuning dynamics*

The periodic injection-current waveform used to modulate the laser impacts its wavelength-tunability and power-output characteristics. At very high scan rates, a sinusoidal waveform is commonly used for injection-current modulation, which gradually changes the heating applied to the laser between a maximum and minimum value. The harmonics of sinusoidal modulation may also be conveniently analyzed [9]. Here we rigorously examine the benefits and potential drawbacks of square-waveform modulation, which has previously shown some benefit to improving optical SNR for under-sampled spectra [35]. In square-wave modulation, the laser heating no longer changes gradually. Instead, during the upscan, a step change to maximum current and heating occurs, and during the downscan, the maximum level of cooling occurs when the current changes step-wise to the minimum value. These dramatic variations of heating and cooling allow the laser grating to reach greater extremes of temperature, resulting in greater spectral scan depth. For the present setup, applying a sine wave which is scanned between the lasing threshold (approximately 110 mA) and the maximum allowable current (190 mA), a scan depth of 0.40 $\mathrm{cm}^{-1}$ is achievable. With a square wave operating with the same current amplitude, a scan depth of 0.57 $\mathrm{cm}^{-1}$ is achievable, representing a significant increase of ∼43%, which corresponds closely to the predictions from Eqs. 35 and 61. The aforementioned sinusoidal and square waveforms are indicated in the first two columns of Fig. 2.

Beyond the increase in scan depth due to the waveform change, it is clear that the optical signal-to-noise ratio (SNR) associated with the laser output increases with the square wave, as the laser ramps up to its maximum output power much more quickly and for longer in time than for a sine wave. Additionally, compared to the sine wave modulation, the optical SNR remains roughly constant across the scan, mitigating bias of the spectral measurement between regions of high and low optical SNR. It should be noted that square-wave modulation necessarily results in the downscan having near-zero optical SNR. However, as mentioned in Section 2, for MHz-rate modulation, even for sinusoidal waveforms,

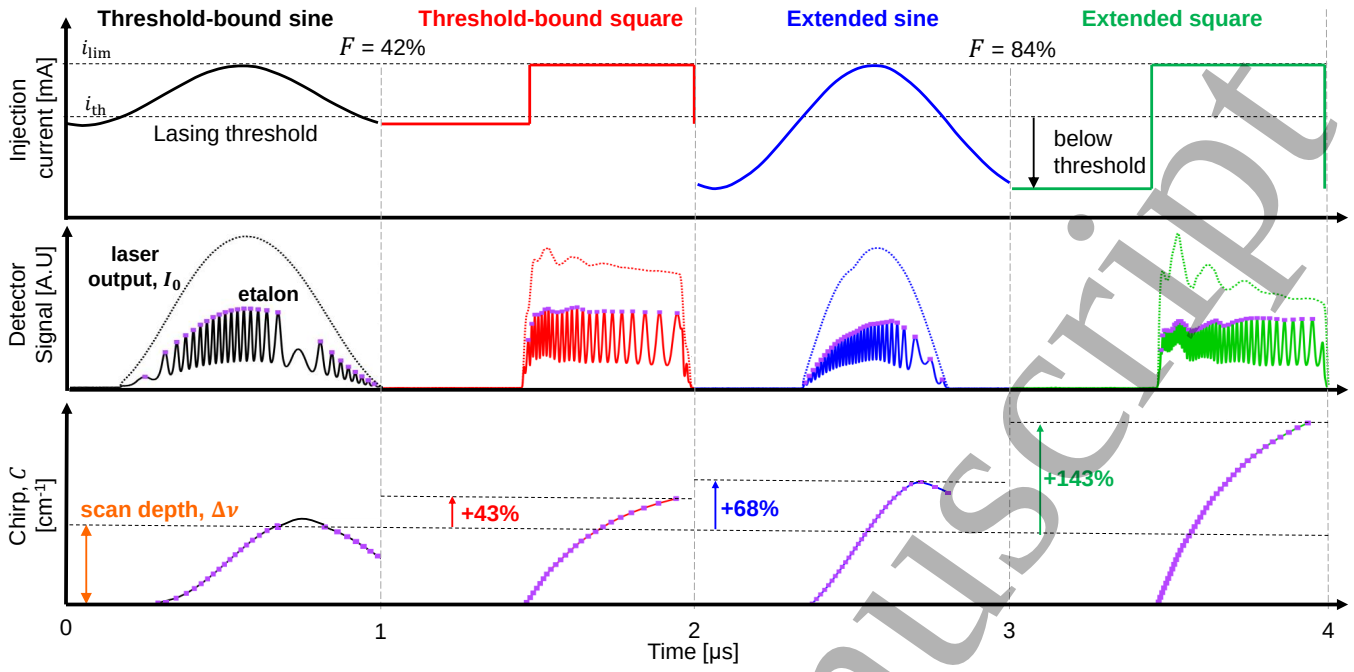


**Fig. 2** *Top*: Injection current *versus* time for various MHz waveforms. *Middle*: Detector signals produced by laser output (dotted curves) and signal when germanium etalon in beam path (solid curves). *Bottom*: Inferred laser chirp *versus* time (solid curves) obtained from the etalon signal peaks (purple dots).

the downscan already typically has poor optical SNR due to the lag between wavelength and intensity modulation and is consequently not usually utilized for spectral information.

In addition to square-wave modulation, and by a similar principle, scan depth was shown to increase by modulating below the lasing threshold current. In this case, the amplitude of the modulated current signal was extended to span between near-zero current and the maximum current limit of the laser. This technique increases heat dissipation and causes the amplitude of the temperature modulation to increase, which explains why the scan depth increases, despite the fact that the observed intensity is lower as the laser is not outputting light when it is scanned below the lasing threshold. We normalize the peak-to-peak current amplitude $i_{pp}$ by the maximum current amplitude $i_{pp,max}$ (modulating from zero current to the current limit) to define a variable termed the *fractional current*, $F$:

$$F = \frac{i_{pp}}{i_{pp,max}} = \frac{i_{pp}}{i_{lim}} \tag{5}$$

For the laser used in this work, scanning between the lasing threshold and maximum current limit corresponds to a *threshold-bound* fractional current of $F_{th} = 42\%$. In other words, the fraction of injection-current range (from zero to max current) for which lasing occurs is 42%, and the current range below the threshold represents the other 58%. To mitigate the risk of reverse-biasing the laser, a minimum current limit value was set at approximately 1/3 of the lasing threshold current (30 mA for this work) corresponding to a maximum fractional current of $F = 84\%$. The injection-current profiles for these two values of fractional current are shown in Fig. 2, with the first two columns featuring waveforms at $F_{th} = 42\%$ and the second two columns featuring waveforms at $F = 84\%$. For the remainder of the paper, to emphasize the improved scan depth of this technique, we will call waveforms with $F > F_{th}$ "extended", i.e., *extended sine* or *extended square*. Waveforms that are modulated between the lasing threshold and current limit ($F = F_{th}$) are termed "threshold-bound". The effect of the fractional current variation

**Table 1** Variation of the scan depth as a function of fractional current from 42% (threshold-bound) to 84% (extended).

| **Fractional current, $F$ [%]** | **Scan depth, $\Delta\nu$ [cm$^{-1}$]** | |
|---|---|---|
| | Sine wave | Square wave |
| 42 (threshold-bound) | 0.40 cm$^{-1}$ | 0.57 cm$^{-1}$ |
| 84 (extended) | 0.64 cm$^{-1}$ | 0.99 cm$^{-1}$ |

can be directly seen in Table 1. When the waveforms are modulated at the maximum fractional current, the scan depths increase to 0.64 cm$^{-1}$ for the sine wave, and 0.99 cm$^{-1}$ for the square wave. This represents a 60% and 148% increase respectively in scan depth compared to the threshold-bound sine wave modulated at the threshold-limited fractional current modulation.

An interesting and notable side effect of the MHz-rate current modulation below the lasing threshold is an

effective extension of the temperature tuning range of the laser. DFB lasers are typically designed to operate in a range of wavelengths limited by the temperature range achievable by the Peltier TEC. We observed that extended current modulation at high speeds allows for the DFB-QCL to lase at wavenumbers that would otherwise be inaccessible. Typically, when the current applied to the laser decreases, the wavenumber output of the laser increases (wavelength decreases) as the laser drops in temperature. When the current drops below the threshold current, the laser continues to cool, tuning the laser DFB grating to higher wavenumbers. However, these frequencies of light are not outputted by the laser, as the laser power drops to zero below the lasing threshold. In the case of high-speed modulation, however, the lag between the laser intensity output and the laser temperature allows for the laser cavity to be tuned to a wavenumber associated with a "below-threshold" temperature while the power is quickly ramped up above the threshold. By shifting the fractional current from $F = 42\%$ to $F = 84\%$ the spectral domain accessible by the laser was effectively extended by $\sim$1.5 cm$^{-1}$, which is equivalent in this case to shifting the laser TEC setpoint $\sim$10°C colder.

In addition to the influence of waveform shape and fractional injection-current amplitude, the effects of injection-current duty cycle were also examined, specifically for the square waveform. As the duty cycle is varied, there is a tradeoff between the amount of time spent heating and cooling the laser. For instance, a duty cycle above 50% involves longer periods of heating than cooling, and the opposite for a duty cycle below 50%. In Fig. 3, representative laser output intensity traces are shown for three square waves of varying duty cycle (20%, 50%, and 80%) which all share a fractional current of 42%. As might be expected, the spectral scan depth is maximized for a duty cycle of 50%, which agrees with observations made by Chrystie et al. for pulsed QCLs [30]and is supported by the mathematial arguments presented in the appendix. The variation of the scan depth with duty cycle can be seen with the black curve in Fig. 4 for extended waveforms with $F = 84\%$.

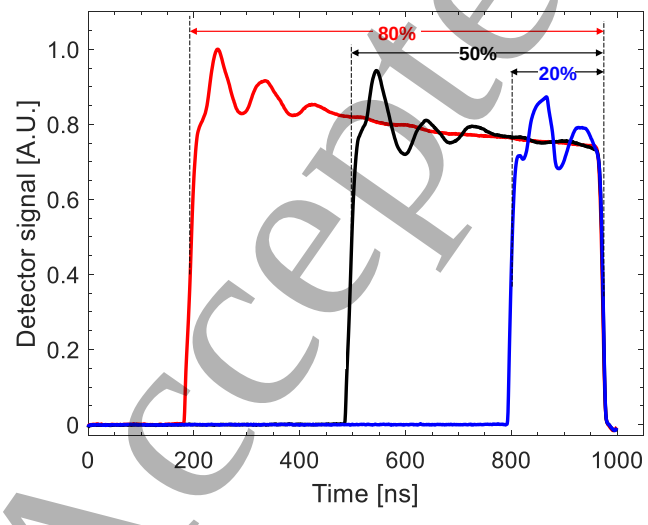


**Fig. 3** Detector signals for extended square waves ($F = 84\%$) with varying duty cycle.

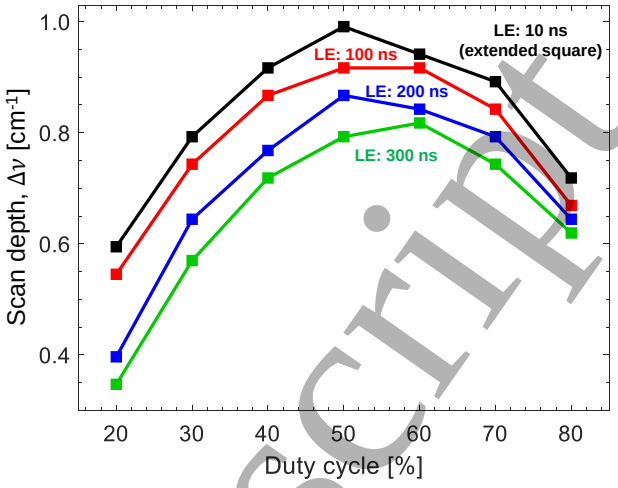


**Fig. 4** Scan depth *versus* duty cycle for extended square waveforms ($F = 84\%$) varying leading-edge (LE) ramp times.

It should be noted that the aforementioned effects are pronounced at very high scan rates because chip heating and cooling are too slow to change to a fixed wavelength (top of square wave) within the scan period. At slower scan rates, the spectral scan depth would presumably be less sensitive to duty cycle, as the laser would likely be able to reach the output wavelength associated with maximum current level, regardless of the time spent in the upscan relative to the downscan. Accordingly, as laser scan rate is reduced, the relative gain in spectral scan depth would be reduced. Additionally, it should be expected that the thermal responsivity and heat dissipation rates vary from one laser chip to another, but in the examination of several CW-DFB lasers in our laboratory, similar effects (with regards to the gain in spectral scan depth) on the same order of magnitude were observed under MHz modulation. We further note that the relative gain from sub-threshold extended current modulation depends on the baseline fractional threshold current. Specifically, DFB interband cascade lasers (ICLs) typically have lower threshold current values relative to their maximum current limit compared to quantum cascade lasers. This means that the threshold-limited fractional current for these lasers are typically high ($> 60\%$) relative to QCLs. As such, the opportunity for spectral scan depth improvement via extended scanning is limited for these types of lasers. As an example, for a Nanoplus ICL with an output wavelength near 4.19 µm tested in our laboratory, the threshold-limited fractional current was 75%. The spectral scan depth increased 32% for a square waveform when increasing the fractional

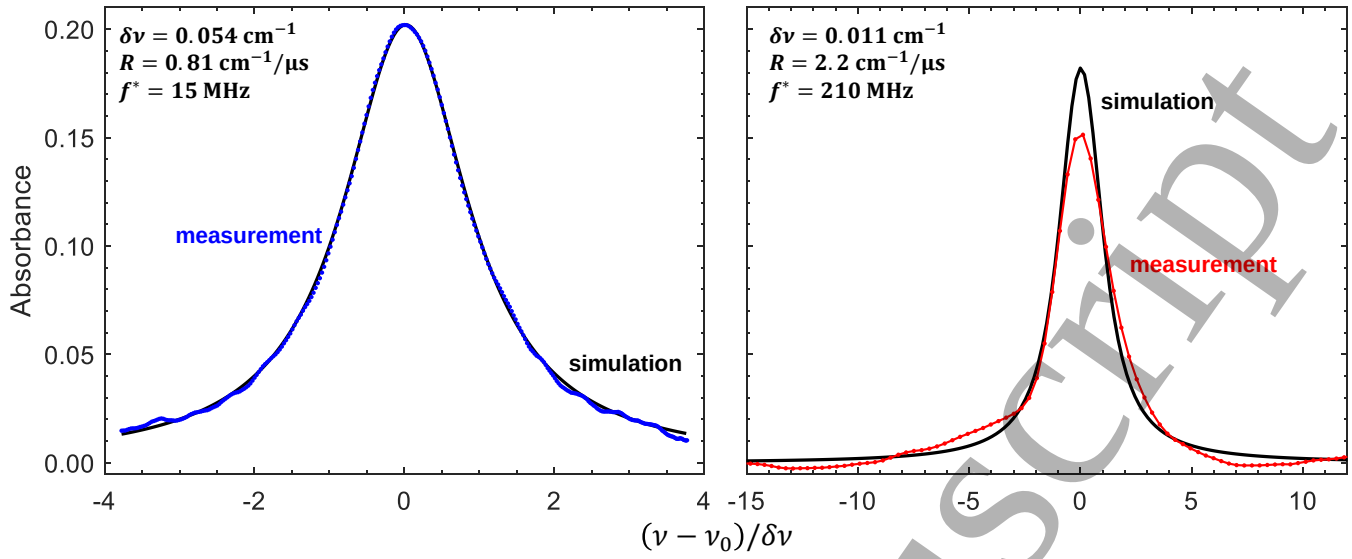


**Fig. 5** Absorbance measurement of the $^{12}C^{16}O$ P(0,22) line *versus* wavenumber normalized by the linewidth (relative to linecenter). *Left*: Close agreement between low characteristic frequency measurement (15 MHz, blue) and a Voigt profile simulation (black). *Right*: Lineshape distortion of high characteristic frequency measurement (210 MHz, red) compared to a Voigt profile simulation (black).

current from 75% to 95%. However, square-wave modulation was still greatly beneficial relative to sine-wave modulation for this same ICL, with the threshold-bound square wave having 72% higher spectral scan depth relative to a threshold-bound sine wave.

### *3.2 Detection bandwidth limitations*

The aforementioned methods for extending the spectral scan-depth capability of DFB lasers can generate optical signals with very high temporal frequency content, and thus spectral resolution may become limited by the detection system. If the frequency content of the optical signal is near or above the detection-system bandwidth (related to the bandwidth of the detector and oscilloscope), then the recorded signal can become distorted as the high-frequency components of the signal become attenuated and phase-shifted due to effective low-pass frequency filtering. Distortion of the background or transmitted light intensity causes the measured absorbance (obtained using Eq. 4) to be similarly distorted. An example of such a distorted absorbance measurement is shown on the right side of Fig. 5.

High frequency content in the optical signals may come about due to (1) fast scanning across a narrow spectral feature when making an absorption measurement ($I_{tr}$ distortion) or (2) high-frequency oscillation of the raw laser output intensity ($I_0$ distortion). Narrow spectral features can cause rapid changes in transmitted light intensity as the laser wavelength rapidly scans across the feature. This type of distortion will occur when either the spectral features have a narrow linewidth $\delta\nu$ [$cm^{-1}$] or when the rate of change of the laser output wavenumber is high. The magnitude of the rate of change of wavenumber output (or chirp, $C$) of the laser is termed the "chirp rate", $R$ [$cm^{-1}s^{-1}$] [19]:

$$R = \left|\frac{d\nu}{dt}\right| = \frac{dC}{dt} \tag{6}$$

For infrared absorption spectra of small gaseous species (i.e. CO, $CO_2$, $H_2O$) at near-atmospheric pressures, the dominant contributor to the linewidth is collisional broadening ($\delta\nu \approx \delta\nu_C$) [36] which scales linearly with gas pressure. As such, the bandwidth related distortion will be pronounced at lower pressures. It is postulated that for a given detector bandwidth, there will be a maximum "characteristic frequency" $f^*$ [Hz] associated with the light intensity change due to the narrow spectral absorption feature:

$$f^* = \frac{R}{\delta\nu} \tag{7}$$

Here, $\delta\nu$ is the full-width half maximum (FWHM) of the target spectral feature. Equivalently, a "characteristic time" $\tau^*$ [s] may be defined which intuitively represents the time required to scan the FWHM of the spectral feature:

$$\tau^* = \frac{1}{f^*} = \frac{\delta\nu}{R} \tag{8}$$

In order to identify the maximum allowable characteristic frequency for the target line used in this work with a 200-MHz bandwidth detection system, a series of measurements of carbon monoxide (CO) absorption at room temperature were conducted by placing a 33.94-cm static gas cell into the optical path. This gas cell was filled with pure CO to various fill pressures. Before the cell was filled, we measured the background intensity

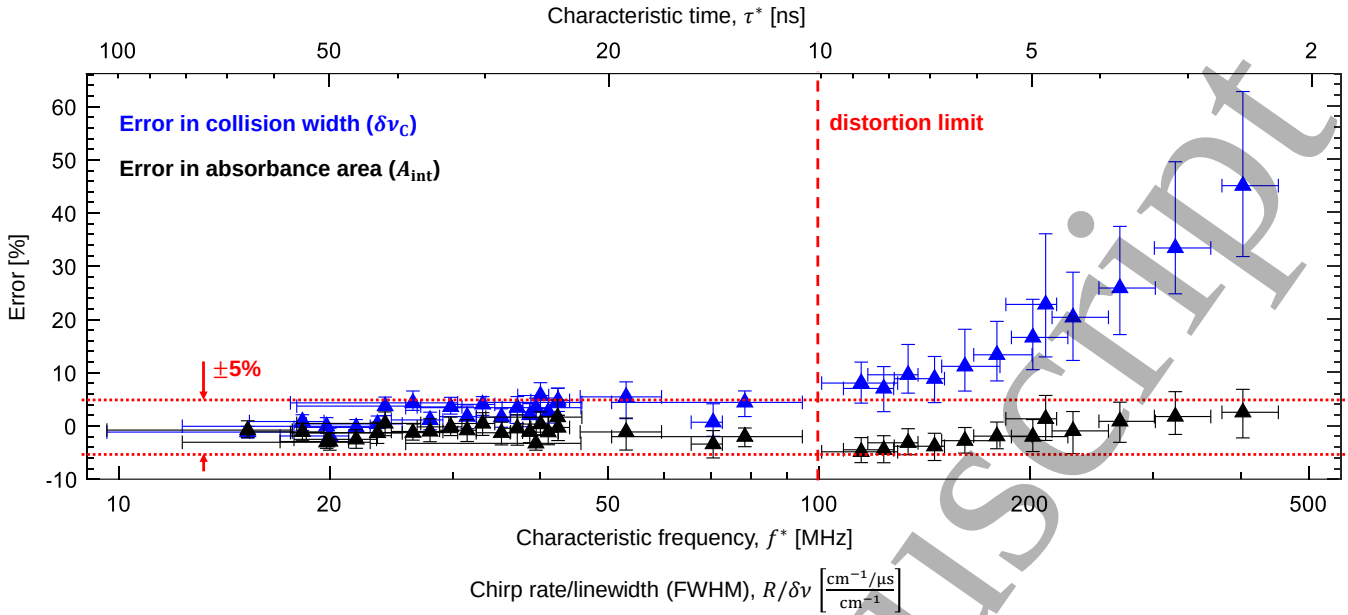


**Fig. 6** Error in fitted collision linewidth and absorbance area of the $^{12}C^{18}O$ P(0,22) line at various characteristic frequencies (chirp rate over FWHM). The error in the fit of $\delta\nu_C$ is seen to increase significantly past $f^* = 100$ MHz

with and without the etalon in the beam path, to transform the results from the time domain to the spectral wavenumber domain. After the cell was filled, the transmitted light intensity was recorded, and an absorbance measurement was calculated using Eq. 4. The laser's center wavelength was tuned to the P(0,22) line of $^{12}C^{18}O$ at 2004.28 cm$^{-1}$, which was selected due to its isolation from other CO lines and from the spectra of ambient water. Measurements were performed using sine waves in order to isolate the effects of the potential high-frequency content in other waveforms. The chirp rate of these sine waves was adjusted by varying the fractional current and the laser modulation frequency. In addition, the characteristic frequency of the measurement is adjusted by filling the gas cell to different pressures, resulting in variation in the FWHM of the spectral feature.

Sample room-temperature absorbance measurements are shown in Fig. 5. A range of characteristic frequency measurements were collected spanning from 10 MHz to 400 MHz. At low characteristic frequencies, the measured absorbance spectra agrees closely with a Voigt simulation of the target line using linestrength and self-broadening parameters from HITRAN 2020 [37], as indicated on the left side of Fig. 5. At high characterstic frequencies the measured lineshape becomes distorted, as indicated on the right side of Fig. 5. There is a reduction in the measured peak absorbance, along with signal artifacts in the wings of the line. This distortion precludes accurate fitting of the absorption lineshape.

In order to assess the magnitude of the detector induced distortion on the measured lineshape parameters, a Voigt profile [38] was fitted to the measured spectra over a range of characteristic frequencies. In this lineshape fitting routine, the Doppler linewidth of the Voigt profile was fixed whereas the collision linewidth ($\delta\nu_C$), absorbance area ($A_{int}$ [cm$^{-1}$]), and absolute line position of the line were allowed to float. The three parameters were varied until a solution minimizing the sum of squared errors between the measurement and fit was found. The error in fitted collision linewidth and absorbance area is plotted in Fig. 6 against the characteristic frequency of the absorption measurement. It can be seen that for lower characteristic frequencies, the error in the measured spectral parameters is low and on the order of the scan-to-scan variation in the error, as indicated by the vertical error bars. At higher frequencies however, the fitted collision width ends up being higher than the true collision width, revealing in an instrument-induced broadening of the line. It is interesting to note that the fitted absorbance area is more robust to the detector induced distortion, with the error in the fitted areas staying within ±5% even at the highest tested characteristic frequencies. The critical characteristic frequency beyond which the collisional linewidth measurement error exceeds 5% is approximately 100 MHz (corresponding to $\tau^* = 10$ ns), which is 1/2 the detection system bandwidth $f_{BW} = 200$ MHz, implying that the following criteria should be met to mitigate detector induced distortion of absorption signals:

$$f^* < \frac{1}{2} f_{BW} \tag{9}$$

The above criteria may be used to establish a maximum allowable laser chirp rate for a given detection system bandwidth and target spectral feature. For example, if the $^{12}C^{16}O$ P(0,22) line was to be measured down to pressures of 0.25 atm ($\delta\nu = 0.027$ cm$^{-1}$) using a 200-MHz bandwidth detection system, a maximum allowable

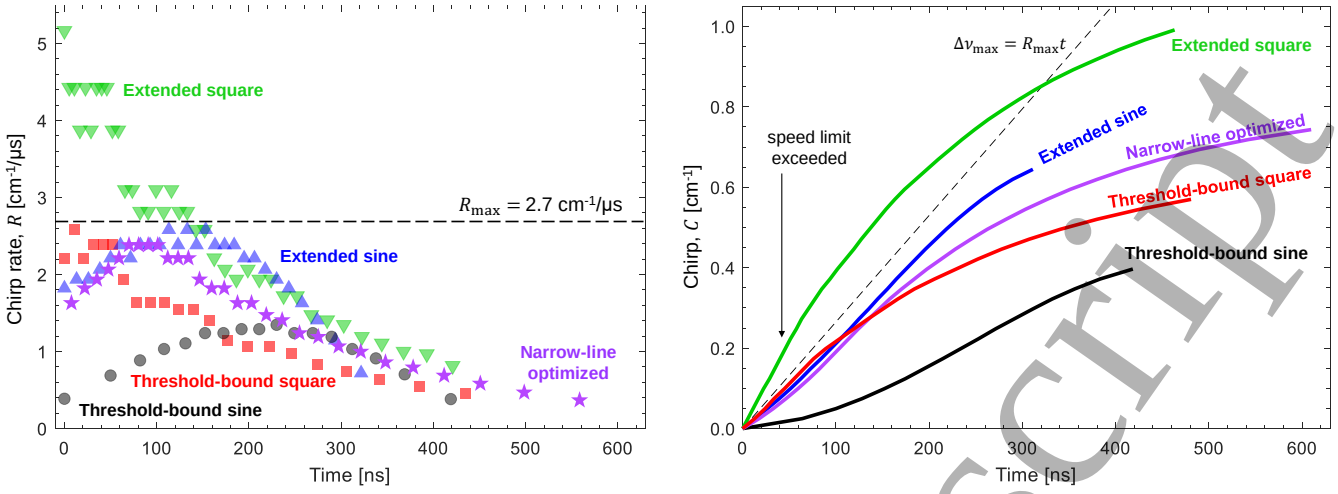


**Fig. 7** *Left*: Chirp rate *versus* time for the threshold-bound sine, threshold-bound square, extended sine, extended square, and optimized waveform. The extended square is observed to exceed the chirp-rate limit defined for scanning CO at 0.25 atm (2.7 $\text{cm}^{-1}/\mu\text{s}$). *Right*: Chirp *versus* time for the same waveforms. The extended square yields the highest scan depth but exceeds the bandwidth-limited chirp rate. The optimized waveform achieves high scan depth while remaining below the speed limit.

measurement error of 5% imposes a maximum chirp rate of $R_{\max} = 2.7\ \text{cm}^{-1}/\mu\text{s}$. In light of this limit, the waveforms discussed in Section 3.1 can be re-evaluated. The left side of Fig. 7 indicates the chirp rate versus time during a single modulation period for the various waveforms. Some of these waveforms resulted in chirp rates that exceeded this limit during some portion of the scan. We can define a usable scan depth, $\Delta\nu_{\text{use}}$, which corresponds to the scan depth, $\Delta\nu$, restricted to the portion of the scan where the chirp rate is below $R_{\max}$:

$$\Delta\nu_{\text{use}} = \Delta\nu\big|_{R<R_{\max}} \tag{10}$$

For the threshold-bound sine wave ($F = 42\%$), the extended sine wave ($F = 84\%$), and the threshold-bound square wave ($F = 42\%$), the chirp rate never exceeds the maximum allowable value. Thus, their usable scan depths are equal to the actual scan depths. However, for the extended square wave, the chirp rate does exceed the limiting value at the beginning of the upscan, meaning that spectral features positioned at the beginning of the scan could be potentially distorted. The usable scan depth for the extended square is therefore reduced from 0.99 $\text{cm}^{-1}$ to 0.50 $\text{cm}^{-1}$, rendering it less useful than the threshold-bound square wave and extended sine, for this particular narrow-linewidth absorption. In fact, when considering usable scan depth, maximizing $F$ does not maximize $\Delta\nu_{\text{use}}$. For a square wave, the usable scan depth is similar for fractional current values between 40 and 65%, yielding an approximate usable scan depth of 0.5 $\text{cm}^{-1}$. The chirp versus time for the aforementioned waveforms during a single modulation period are indicated on the right side Fig. 7. A dashed line is plotted with the slope equal to the maximum chirp rate. This corresponds to the maximal chirp achievable while respecting the bandwidth-limited chirp-rate limit. The extended square clearly overtakes this maximal chirp profile at early times. It must be noted that for FWHMs above ~0.05 $\text{cm}^{-1}$ (corresponding to pressures above ~0.5 atm for CO), the full extended square waveform (with 0.99 $\text{cm}^{-1}$ scan depth) can be used without an expected distortion of the spectra—limitations on the broad tuning offered by this technique are only relevant for measurements of narrow spectral features.

The other potential source of high-frequency content relates to the oscillations in raw laser intensity. This appears as a *ringing* at the beginning of a scan due to the overshoot in laser output power when the injection current undergoes a large step-change, on the order of nanoseconds [39, 40], induced by the square waveform (which can be related to the Gibbs phenomenon). Ringing can be observed at the beginning of the various square-wave pulses shown in Figs. 2 and 3. The amplitude of ringing increases as the fractional current is increased because the laser current is changing more drastically. For the laser studied in this work, it was found that the ringing frequency was on the order of 10 MHz, which is well below the detection bandwidth of 200 MHz used in this work. Additionally, to validate that the ringing associated with the extended square waveform did not lead to distortion of the measured spectra, room-temperature measurements of CO at 0.5 atm were conducted across the waveform. In each test, the laser temperature was tuned to position the spectral feature at various positions along the scan waveform. Whether or not the feature was positioned in a region of high ringing, the error in the measured absorbance area and collision width was below 5%, validating the lack of ringing-induced distortion. When ringing is present in the background signal, proper temporal alignment of the background and transmitted intensity profiles must

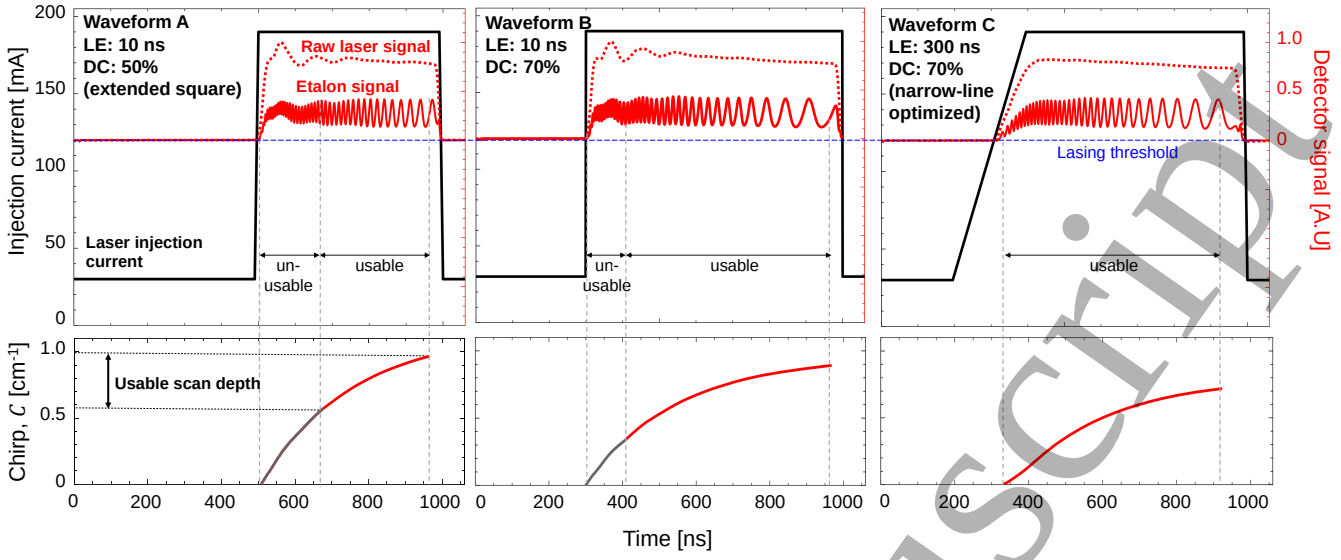


**Fig. 8** Laser injection current, detector signals (*top*) and chirp profiles (*bottom*) for a 10 ns leading-edge square waveforms with 50% duty cycle (waveform A, *left column*) and 70% duty cycle (waveform B, *middle column*). The narrow-line optimized trapezoidal waveform with a 300-ns ramp and 70% duty cycle (waveform C) is shown in the right column. The combined effect of the leading-edge ramp and increased duty cycle keep the chirp rate below the detector limit, making the entire scan usable.

be enforced. Otherwise, the absorbance signal will include non-trivial baseline artifacts that are difficult to remove in post-processing techniques. On the other hand, the absence of these residual artifacts is a good indicator of proper alignment or phasing between the incident and transmitted light intensities when calculating absorbance—this utility is not typical of conventional waveforms. Ringing also results in a loss of potential optical SNR due to the short-lived nature of the peak laser intensity. In the next section, we will show that an optimal compromise between the extended sine and the extended square can be found using arbitrary waveform generation to mitigate ringing and detection-system induced distortion while maximizing optical SNR and scan depth.

### *3.3 Waveform optimization*

It is clear that the extended square waveform maximizes spectral scan depth, but high initial chirp rates and ringing can reduce the usefulness of the full waveform. To mitigate the limitations of detector bandwidth for narrow spectral-feature detection and reduce ringing, one can presumably slow the initial rate of change of the laser output power and output frequency. One method to accomplish this involves modifying the duty cycle of the waveform. As discussed in Section 3.1, spectral scan depth is optimized at a duty cycle of 50%. However, increasing the duty cycle has the effect of reducing the amount the laser cools during the downscan. This makes the temperature change at the beginning of the upscan less drastic, reducing the chirp rate, leading to more of the scan being usable. This effect can be seen in the left and middle columns of Fig. 8, where square pulses with duty cycles of 50% and 70% are compared. The increase in the duty cycle increases the usable scan depth from 0.42 $\text{cm}^{-1}$ to 0.52 $\text{cm}^{-1}$. On the other hand, reducing the duty cycle causing the laser temperature to drop more significantly during the downscan, causing more rapid heating during the beginning of the upscan leading to high initial chirp rates, reducing the usable scan depth. This is exacerbated by the short duration of the upscan, meaning that there is minimal time for the laser chirp rate to return to slow enough speeds. In fact, at 20% duty cycle, the usable scan depth is zero.

Increasing the waveform duty cycle improves usable scan depth to a point, and additional gains can be made by adding a linear ramp to the beginning of the pulse, turning the square into a trapezoid. The length of the ramp has a maximum value for a given duty cycle, as detailed in the appendix. When using a ramp, the definition of duty cycle is the fraction of the scan period for which the current is above the midrange value, $i_{\text{mid}}$, which is the arithmetic mean of the maximum and minimum current. This ramp has the effect of providing more gradual heating to the laser, resulting in slower initial wavelength tuning while also mitigating ringing in the optical output signal. This effect can be seen in the right column of Fig. 8 where a 300-ns leading-edge ramp is added to the waveform with 70% duty cycle. As the length of the leading-edge ramp is increased, the overall scan depth achieved by the laser is necessarily reduced, along with a reduction in optical SNR during the initial part of the scan. At 50% duty cycle, changing the leading edge ramp does not improve the usable scan depth, as the reduction in initial chirp rates is almost exactly com-

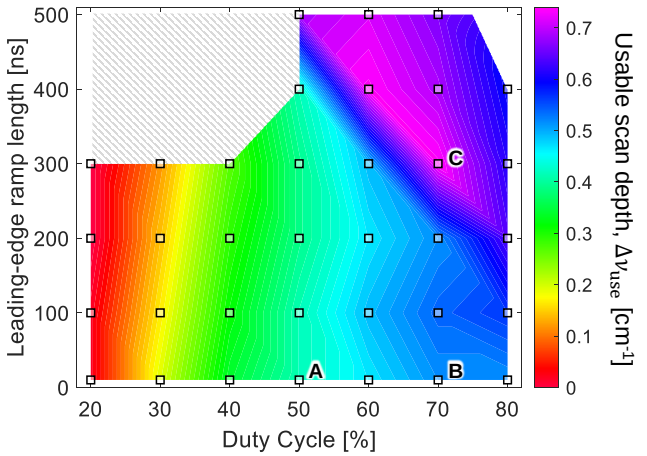


**Fig. 9** Contour plot of usable scan depth as a function of duty cycle and leading-edge ramp length at a fixed fractional current $F = 84\%$. The points A, B, and C correspond to waveforms A, B, and C from Fig. 8, with point C (narrow-line optimized waveform) clearly corresponding to a waveform of high usable scan depth. The gray region in the top left corner of the plot represents waveforms that were not investigated due to sub-optimal usable scan depth.

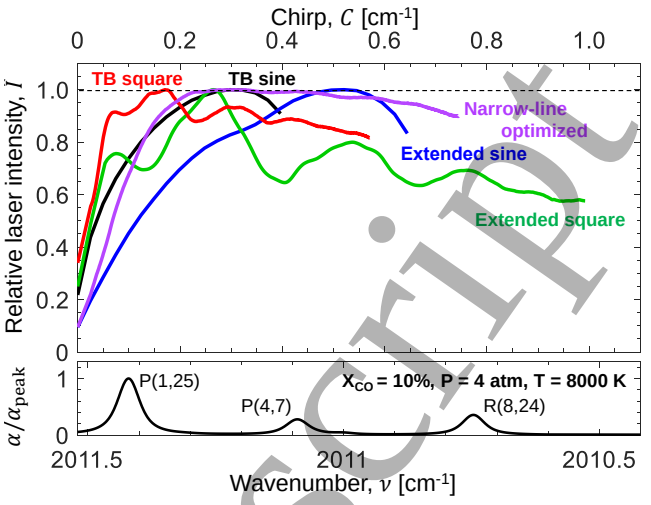


**Fig. 10** *Top*: Normalized laser power *versus* chirp for the various waveforms ("TB" refers to threshold-bound waveforms). *Bottom:* Sample absorbance spectrum of 10% CO in air near 5 µm at 4 atm, 8000 K.

pensated by the reduction in overall spectral scan depth. On the other hand, at higher duty cycles, the addition of a leading-edge ramp improves the usable scan depth for narrow-line measurement. For the 70% duty-cycle waveform, shifting from a 10 ns ramp to a 300 ns ramp boosts the usable scan depth from 0.52 cm$^{-1}$ to 0.74 cm$^{-1}$. The entire scan also becomes completely usable, as the chirp rate limit is not exceeded at any point. It is also interesting to note that as the length of the leading-edge ramp is increased the optimal duty cycle for maximizing overall spectral scan depth also shifts to higher values than 50%. This effect can be seen in Fig. 4 and a physical explanation for this phenomenon is presented in Section A.5 of the appendix.

In order to find a trapezoidal waveform that maximizes usable scan depth while $R_{max} < 2.7$ cm$^{-1}$ (for narrow-spectra measurement), a multi-parameter optimization was conducted. Laser output intensity and etalon signal were recorded for the various trapezoidal waveforms and the scan depth and peak chirp rate were identified for each waveform. The usable scan depth was mapped as a function of the leading-edge ramp time (varied in increments of ~100 ns), duty cycle (varied in increments of 10%), and fractional current. A contour plot of the variation in usable scan depth with duty cycle and leading-edge ramp time at a fixed value of fractional current ($F = 84\%$) is shown in Fig. 9. The aforementioned trends of improved usable scan depth at increased duty cycle and leading-edge ramp times can clearly be observed. The usable scan depth maximized at a value near $\Delta\nu_{use} = 0.74$ cm$^{-1}$ in a region where duty cycle is 60–70% and the leading edge ramp time is 300–400 ns and the maximal fractional current $F = 84\%$. Given this range of options, the waveform with the longer duty cycle and shorter leading edge ramp is chosen (DC = 70% and LE = 300 ns) as this choice maximizes optical SNR and increases the length of the scan, enabling higher temporal resolution of the target spectra at a fixed measurement sampling rate. This optimized waveform is termed the "narrow-line" optimized waveform.

The chirp rate and chirp profiles for this waveform are compared to the other waveforms in Fig. 7. The injection-current profile, laser output intensity, etalon signal, and chirp versus time are shown on the right side of Fig. 8. Figure 10 compares the chirp and laser output intensity profiles (normalized by peak intensity to obtained the *relative intensity* $\hat{I} = I/I_{peak}$) of the various waveforms. The effect of the scan depth variation in the waveforms can also be observed in relation to a sample spectrum of high-temperature CO, where the higher scan-depth waveforms are able to scan across more transitions. It can be clearly seen that the optimized waveform does not induce ringing in the laser power output. This allows for an increase in the optical SNR of measurements with this profile, as the laser spends more of its time at peak power compared to the cases with ringing, where the laser is only momentarily at the maximum power output. This compensates for the initial reduction in optical SNR over the first 0.2 cm$^{-1}$ of the scan. This can be assessed quantitatively by finding the spectrally-averaged relative laser power $\overline{I}$ across the scan:

$$\overline{I} \equiv \frac{1}{\Delta\nu}\int_0^{\Delta\nu} \hat{I} dC \qquad (11)$$

The values of $\overline{I}$ for the main waveforms studied in this work are included in Table 2. The narrow-line optimized waveform has the highest value of $\overline{I}$, which is indicative of how long the waveform spends at maximum power.

**Table 2** Comparison of the average laser intensity metrics for the various waveforms in this study. NL refers to"narrow-line".

| Waveform | $\overline{I}$ | $\overline{\Delta\nu}$ [cm$^{-1}$] | $\overline{\Delta\nu}_{\text{use}}$ [cm$^{-1}$] |
|---|---|---|---|
| TB sine | 0.83 | 0.33 | 0.33 |
| Extended sine | 0.76 | 0.49 | 0.49 |
| TB square | 0.87 | 0.50 | 0.50 |
| Extended square | 0.71 | 0.71 | 0.42 |
| NL optimized | 0.88 | 0.65 | 0.65 |

To incorporate the effect of scan depth on this power analysis, another figure of merit, the "weighted scan depth" $\overline{\Delta\nu}$ may be defined, which integrates the relative laser intensity $\hat{I}$ over the the chirp of the laser, which is the product of $\overline{I}$ and $\Delta\nu$:

$$\overline{\Delta\nu} \equiv \int_0^{\Delta\nu} \hat{I} dC = \overline{I}\Delta\nu \tag{12}$$

This is essentially the scan depth of the laser, weighted by the relative laser output intensity across the scan and can be visualized as the area under the curves in Fig. 10. $\overline{\Delta\nu}$ is also tabulated in Table 2 for the various waveforms analyzed in this work. The narrow-line optimized waveform, has a value of $\overline{\Delta\nu}$ only 6% lower than the value for the extended square, despite the fact that the optimized waveform scan depth is 20% lower. The spectral information collected with the optimized waveform is therefore of higher average optical SNR than the extended square. If only integrating over the usable part of the scan in a sensing application involving narrow spectra features, a "weighted usable scan depth" $\overline{\Delta\nu}_{\text{use}}$ can also be defined. This is also tabulated in Table 2, which indicates a 55% improvement with the narrow-line optimized waveform over the extended square. While neither $\overline{I}$, $\nu$, nor $\nu_{\text{use}}$ are used in the waveform optimization procedure presented above, they may be incorporated in future optimization for sensing strategies where optical SNR is of high importance, such as for the measurement of optically thick/thin spectra or in power limited applications.

The previous analysis reveals that the key constraint in waveform optimization is the maximum allowable chirp rate. This maximum chirp rate is obtained using Eqs. 7 and 9 based on the detection system bandwidth and the linewidth of the target spectral features. Notably, the maximum allowable chirp rate can be increased by using a higher bandwidth detection system or by targeting broader spectral features. By considering these two parameters, waveforms with maximum useful scan depths can be employed without spectral distortion. It should be noted that the analysis here used a specific but representative quantum cascade laser. For other CW-DFB lasers, a different optimum point may exist with varying scan depth and chirp profiles, but the same general trends and principles are expected to apply. Waveform variations beyond adding a linear ramp were not explored for the sake of simplicity, but it is possible that a more complex waveform could yield further improvements . These waveforms would likely follow the dashed chirp profile from the right side of Fig. 7.

### *3.4 Sensing demonstrations*

*3.4.1 Dynamic pressure measurements* To demonstrate the utility of the high scan depth offered by the extended square waveform ($F$ = 84%, DC = 50%, and LE = 10 ns), MHz-rate LAS measurements of gas pressure were performed in a dynamic combustion environment. The experiment was conducted on UCLA's Detonation Impulse Tube (DIT) facility [17]. In these experiments, a mixture of stoichiometric ethylene ($C_2H_4$) and oxygen ($O_2$) at an initial pressure of 207 Torr was spark ignited at one end of a 196-cm long, 3.81-cm ID tube with a Schelkin Spiral to aid in deflagration-to-detonation transition (DDT). DDT was confirmed via wave-speed measurements made by piezoelectric sensors located near the end of the tube (1.5–1.8 m from the sparkplug). The wave-speeds were seen to match (within measurement uncertainty) values predicted for an ideal

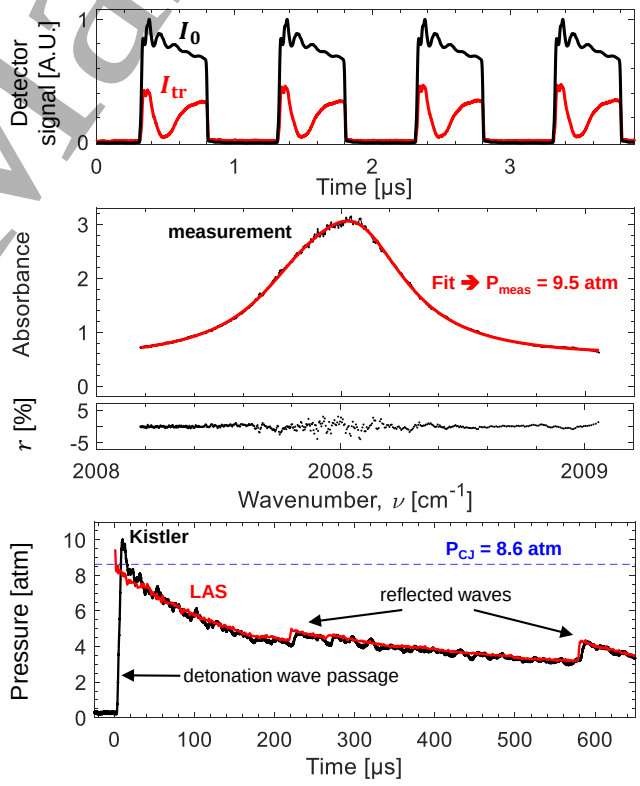


**Fig. 11** *Top*: Measured background (black) and transmitted signals (red) for in detonation tube for the first 4 μs after detonation wave passage. *Middle*: First post-detonation absorbance spectrum (black) along with spectral fit (red). Residuals on the order of $|r| < \pm 3\%$ pictured below (black dots). *Bottom*: Pressure trace obtained using LAS (red) and a Kistler pressure transducer (black) compared to the value computed using CJ detonation theory (dashed line).

1-dimensional Chapman-Jouguet (CJ) detonation wave, as predicted using CalTech's Shock & Detonation Toolbox [41] in CANTERA [42] using the GRI-MECH 3.0 mechanism [43].

The laser discussed in the previous sections is was tuned to target the P(0,31), P(2,20), and P(3,14) rovibrational transitions of $^{12}C^{16}O$ near 2008.5 $cm^{-1}$ with the goal of measuring gas pressure by fitting the measured spectra as in Ref. [7]. During these experiments, the laser light was pitched through the detonation tube via two wedged sapphire windows providing optical access. These windows are located 1.5 m from the spark-plug. Raw laser background and transmitted intensity scans are shown 0–4 µs after the passage of the detonation wave at the top of Fig. 11. A fit of the measured spectra for the first scan after detonation-wave passage is pictured below, which leads to a pressure measurement of 9.5 atm. The residuals between the fit and measurement are generally within ±3%. It should be noted that the raw data are not smoothed in any way prior to fitting. The ringing in the background intensity signal is also present in the transmitted signal, although the magnitude of the signal oscillations is lower due to the high levels of absorption by the combustion gas. The absorbance does not go to zero at the ends of the scan due to the high pressure of the gas which induces significant collisional broadening. Additionally, at high temperatures (>3000 K), there is some broadband interference from $CO_2$ in this spectral region, which causes additional absorption across the scan. This broadband interference is fitted as a constant in fitting procedure and rejected, with the remaining fitted CO Voigt lineshapes being used to solve for the pressure and temperature of the gas.

The time history of the measured gas pressure is shown at the bottom of Fig. 11 at a measurement rate of 1 MHz, without any averaging. The low scatter (measurement SNR∼100)[2] in the measured pressure is a result of the high optical SNR, spectral scan depth, and scan-to-scan stability of the CW laser and the selected injection-current waveforms. The measured peak pressure of 9.5 atm can be compared to the value predicted by the CJ theory obtained using the aforementioned Shock and Detonation Toolbox. This value is indicated as a horizontal dashed line in Fig. 11; close agreement is observed with the measured peak pressure. The measurement also captures decay in pressure from the CJ values after the initial passage of the detonation wave, associated with the Taylor expansion wave [44]. Additionally, the measurement captures the effect of reflected pressure waves resulting from the impact of the detonation wave on the plastic burst diaphragm located at the end of the tube. These reflected waves result in an increase in pressure at the measurement location. The optically-measured pressure dynamics and magnitudes agree very well with the piezoelectric pressure transducer (Kistler 603CAA) located at the same axial plane in the detonation tube. Notably, the large spectral scan depth facilitates measurements at elevated pressure (up to ∼10 atm) at MHz rates.

[2] Measurement SNR is found by taking the ratio of the measured pressure (smoothed using a five-point moving average) and the noise in the pressure signal. The noise of the pressure signal is found by subtracting the pressure signal by the aforementioned five-point moving average and taking the standard deviation of the resulting difference over the same five points.

*3.4.2 Multi-line thermometry* To demonstrate the ability of the extended spectral tuning method to resolve multiple discrete spectral transitions in a 1-µs scan period, a transient multi-line temperature measurement was conducted in the UCLA High-Enthalpy Shock Tube (HEST) facility [24, 45, 46]. In this experiment, 10% CO in argon was shock-heated by a helium driver gas bursting aluminium diaphragms. The driven section of the tube over which the shock forms is 4.9 m long. Optical access is provided by two wedged sapphire windows located 2 cm from the endwall of the driven section. The optical path length through the inner diameter of the tube is 10.32 cm.

Temperature is determined by fitting a simulated spectrum to the measured spectrum of three transitions of $^{12}C^{16}O$ — P(1,25), P(4,7), and R(8,24) — near 2011 $cm^{-1}$ indicated in Figs. 10 and 12. These three lines have a large spread in lower state energies (∼14,000 $cm^{-1}$) and have appreciable absorption strength at temperatures above 5,000 K, enabling sensitive thermometry [34]. In the fitting procedure, temperature, CO number density, line broadening, and absolute line position are varied until the squared sum of the residuals between the measurement and simulation is minimized. The simultaneous fitting of these three lines (rather than two) provides more precise and accurate temperature measurements.

Although having a similar center wavelength and tuning range, the DFB-QCL used in this particular experiment is not the same as discussed in Sections 2–3.4.1. Notably, the achievable scan depth for this second laser is slightly higher, with scan depths up to 1.15 $cm^{-1}$ attainable using the extended square waveform at 1 MHz. Due to the low expected pressures behind the incident shock wave (< 1 atm) and to mitigate ringing, a short leading-edge ramp of 200 ns was added to the waveform. For the present application, the maximum chirp rate was set to 3.5 $cm^{-1}/µs$. Even with this leading-edge ramp added, the scan depth achieved was slightly greater than 1 $cm^{-1}$ at 1 MHz.

Sample raw LAS measurements are shown at the top of Fig. 12 for 0–4 µs after the passage of the reflected shock wave at the measurement location. The absorbance spectrum for the first post reflected shock measurement is indicated in the middle of Fig. 12. Here the full 1-$cm^{-1}$ scan depth enabling three-line detection is readily apparent. Residuals are on the order of ±5%.

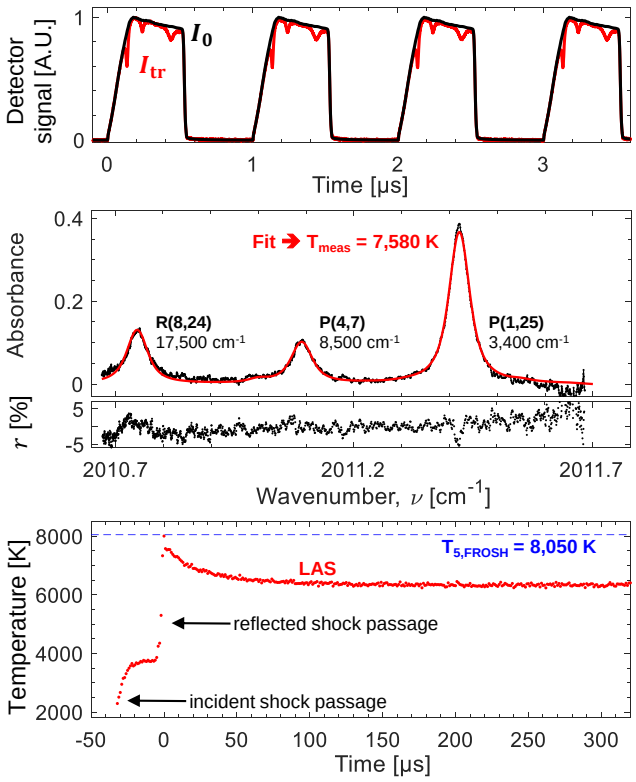


**Fig. 12** *Top*: Measured background (black) and transmitted signals (red) in shock tube for the first 4 μs after the reflected shock wave. *Middle*: 1-cm$^{-1}$ measured absorbance spectrum (black) along with spectral fit (red) for the first post reflected shock measurement. Residuals on the order of $|r| < \pm 5\%$ plotted below (black dots). The names and corresponding lower state energies in cm$^{-1}$ are written next to each major transition. *Bottom*: Temperature time history obtained using LAS (red) compared to post-reflected shock temperature predicted using ideal shock relations (dashed line).

At the bottom of Fig. 12, the temperature versus time is plotted, with time 0 indicating the time of reflected-shock passage at the measurement location. Some vibrational relaxation is observed to occur immediately after the incident shock passage, on the order of 10s of microseconds, with the temperature eventually reaching an equilibrium value near 3760 K. The temperature is rapidly increased to a value near 8010 K across the reflected shock wave. This temperature is in close agreement with the value predicted by ideal shock tube relations [47, 48] of 8050 K. After the reflected-shock passage, the temperature rapidly drops over 10s of microseconds, as CO dissociates. The post reflected shock temperature eventually reaches an equilibrium value of 6350 K. Using this temperature sensing strategy, a measurement SNR of ∼200 is achieved, again as a result of the high optical SNR, spectral resolution, and scan-to-scan stability of the CW laser and the selected injection-current waveforms. The measurement SNR for temperature is found in the same way as for the pressure measurements in Section 3.4.1, using the standard deviation in the difference between the measured temperature and a moving average to find the noise of the temperature signal.

## 4 Summary

Injection-current waveform variations were analyzed for extending and optimizing spectral tuning of CW-DFB lasers via MHz modulation in a bias-tee circuit. Laser chirp rates and signal-to-noise ratio were found to significantly increase by modulating the laser using square waves instead of sine waves and by scanning the laser below the lasing threshold. These techniques ultimately yielded scan depths on the order of 1 cm$^{-1}$ at 1 MHz, representing an increase of more than a factor of 2 relative to threshold-bound sinusoidal modulation. The effect of waveform duty cycle and leading-edge ramp were examined, with a longer leading-edge ramp mitigating output ringing and excessive chirp rate, while requiring a longer duty cycle to maximize useful scan depth. The attenuation of the high-frequency laser signals due to detector bandwidth was also examined, and limiting criteria are defined based on the characteristic frequency of target absorption features. Based on common detector limitations, an optimized trapezoid waveform was established for a 200-MHz bandwidth detection system for use in sub-atmospheric sensing where narrow spectral features are expected. This study revealed that the combination of the bias-tee circuit and injection-current waveform optimization yields more than an order of magnitude gain in temporal frequency (and effective measurement rate) for a target spectral tuning depth (1 cm$^{-1}$) relative to conventional laser modulation via bandwidth-limiting controllers. The various MHz waveform strategies were finally demonstrated for high-speed gas sensing in two impulse facilities. In a detonation tube, we measured transient gas pressure based on collisional linewidth up to ∼10 atm; in a shock tube, we performed dynamic temperature measurements based on three discrete transitions resolvable in a single microsecond modulation period. The analysis presented here may serve as a broadly applicable guide to optimizing injection-current waveform for CW-DFB lasers modulated at MHz rates for absorption spectroscopy.

## Acknowledgements

This work was supported by the Air Force Research Laboratory (AFRL) and OptoKnowledge Systems Inc. under a Small Business Technology Transfer (STTR) program, award no. FA9300-19-P-1503 with Dr. John W. Bennewitz as contract monitor, and Dr. Jason Kriesel as collaborator. Support was also provided by NASA's Space Technology Research Grants Program (award no. 80NSSC21K0066). Supplementary support was provided by the U.S. National Science Foundation (NSF), award no. 1752516 and the Air Force Office

of Scientific Research (AFOSR) Young Investigator Program (YIP) award no. FA9550-19-1-0062 with Dr. Chiping Li as Program Officer. Christopher C. Jelloian is supported by a NASA Space Technology Research Fellowship.

The authors would like to thank Miles Richmond for his assistance running the shock tube experiments, and Dr. Jason Kriesel and Ilya Dunayevskiy of OptoKnowledge Systems Inc. for their support in developing the optical/photonic hardware used in this work. The authors would also like to thank Professor Daniel Pineda for providing insightful feedback and comments on this work.

## A Theoretical analysis of high-speed DFB laser tuning dynamics

In this section we describe a first-order model of DFB laser tuning dynamics which can be used to understand some of the trends observed in the previous sections of this paper. The parasitic components in the laser circuitry (inductance and capacitance) are neglected and the laser output is assumed to be monochromatic. To simplify the laser tuning dynamics, a lumped-element model is used, in which the laser cavity is represented by a single thermal mass at a time-varying temperature $T_\mathrm{L}$ [K]. Two heat transfer terms are included in the model. Ohmic heating from the laser injection current $i(t)$ [A] is modeled as heat transfer into the laser, $Q_\mathrm{in}$ [W]:

$$Q_\mathrm{in} = \rho i^2(t) \tag{13}$$

Here, $\rho$ [$\Omega$] is the equivalent electrical resistance provided by the laser. The cooling provided by the laser heat sink is modeled as heat transfer out of the laser cavity, $Q_\mathrm{out}$ [W]:

$$Q_\mathrm{out} = h(T_\mathrm{L} - T_\mathrm{S}) \tag{14}$$

Here, $T_\mathrm{S}$ is the laser heat sink temperature and $h$ [W/K] is the overall heat transfer coefficient between the laser and heat sink. A key assumption in this first-order analysis is that the heat sink temperature is constant during laser modulation. This assumption becomes increasingly valid as the modulation frequency increases to high rates ($>$ kHz), because the laser heat sink is assumed to have a much larger thermal capacity (mass) than the laser chip. Over longer timescales, such as during static tuning or Hz-rate modulation, the laser heat sink temperature may change and a higher-order analysis may be employed to analyze these situations.

Using the first law of thermodynamics, the change in thermal energy of the laser cavity, $U_\mathrm{L}$ [J], can be expressed with the following energy balance:

$$\frac{dU_\mathrm{L}}{dt} = Q_\mathrm{in} - Q_\mathrm{out} = \rho i^2(t) - h(T_\mathrm{L} - T_\mathrm{S}) \tag{15}$$

By treating the laser as a lumped thermal mass, the rate of thermal energy change of the laser can be expressed in terms of the rate of change of the laser temperature, the thermal mass of the laser cavity, $m_\mathrm{L}$ [kg], and the laser specific heat capacity $c_\mathrm{p}$ [Jkg$^{-1}$K$^{-1}$]. This allows Eq. 15 to be rewritten as a first-order linear differential equation in $T_\mathrm{L}$:

$$m_\mathrm{L} c_\mathrm{p} \frac{dT_\mathrm{L}}{dt} = \rho i^2(t) - h(T_\mathrm{L} - T_\mathrm{S}) \tag{16}$$

The following relationship between laser output wavenumber $\nu$ [cm$^{-1}$] and temperature is adapted from [21], where $\alpha_\mathrm{ex}$ [K$^{-1}$] is the effective thermal expansion coefficient of the DFB grating:

$$\frac{d\nu}{dT_\mathrm{L}} = -\alpha_\mathrm{ex}\nu \tag{17}$$

This equation can be solved to find wavenumber as a function of temperature:

$$\nu = \nu_0 \exp\left[-\alpha_\mathrm{ex}(T_\mathrm{L} - T_{\mathrm{L},0})\right] \tag{18}$$

Here, $\nu_0$ is the laser output wavenumber at an arbitrary reference temperature $T_{\mathrm{L},0}$. As the magnitude of wavenumber changes during laser scanning are relatively minor ($<$1%), this relation may be linearized using a Taylor Expansion:

$$\nu \approx \nu_0 \left[1 - \alpha_\mathrm{ex}(T_\mathrm{L} - T_{\mathrm{L},0})\right] \tag{19}$$

The rate of change of wavenumber with time can also be written as:

$$\frac{d\nu}{dt} = -\alpha_\mathrm{ex}\nu_0 \frac{dT_\mathrm{L}}{dt} \tag{20}$$

Eqns. 19 and 20 can be used to recast Eq. 16 in terms of the laser output wavenumber:

$$\frac{m_\mathrm{L} c_\mathrm{p}}{\alpha_\mathrm{ex}\nu_0}\frac{d\nu}{dt} + \frac{h}{\alpha_\mathrm{ex}\nu_0}\nu = -\rho i^2(t) + h\left(T_{\mathrm{L},0} - T_\mathrm{S} + \frac{1}{\alpha_\mathrm{ex}}\right) \tag{21}$$

The case of static tuning ($d\nu/dt = 0$) can be examined to find the relationship between the reference current $i_0$ and the reference temperature of the laser $T_{\mathrm{L},0}$ which produces the reference output wavenumber $\nu_0$

$$T_{\mathrm{L},0} - T_\mathrm{S} = \frac{\rho}{h} i_0^2 \tag{22}$$

We now define a new variable $\nu_\mathrm{rel}$ as the difference between the output wavenumber and the reference value:

$$\nu_\mathrm{rel} \equiv \nu - \nu_0 \tag{23}$$

We also define a variable termed the "effective heating" $q$ [A$^2$]as the difference in the square of the injection current and the square of the reference injection current:

$$q(t) \equiv i^2(t) - i_0^2 \tag{24}$$

$q$ is the Ohmic heating of the laser chip, normalized by its electrical resistance, with the laser at its reference temperature cooling when $q < 0$ and the laser heating

when $q > 0$. When modulating the injection current, the *heating amplitude* $q_\mathrm{A}$ may be defined as:

$$q_\mathrm{A} \equiv \frac{q_\mathrm{max} - q_\mathrm{min}}{2} = \frac{i_\mathrm{max}^2 - i_\mathrm{min}^2}{2} \tag{25}$$

The heating amplitude may be related to the "fractional current" $F$ from earlier sections:

$$q_\mathrm{A} = i_\mathrm{pp} i_\mathrm{mid} = F i_\mathrm{lim} i_\mathrm{mid} \tag{26}$$

Here, $i_\mathrm{mid}$ is the midrange current:

$$i_\mathrm{mid} = \frac{i_\mathrm{max} + i_\mathrm{min}}{2} \tag{27}$$

Using Eqs. 22 – 24, Eq. 21 can be rewritten in the simplified form:

$$\frac{d\nu_\mathrm{rel}}{dt} + \frac{\nu_\mathrm{rel}}{\tau_\mathrm{L}} = -Bq(t) \tag{28}$$

Here, $\tau_\mathrm{L}$ [s] and $B$ [$\mathrm{cm^{-1}s^{-1}A^{-2}}$] are defined as:

$$\tau_\mathrm{L} \equiv \frac{m_\mathrm{L} c_\mathrm{p}}{h} \tag{29}$$

$$B \equiv \frac{\alpha_\mathrm{ex} \nu_0 \rho}{m_\mathrm{L} c_\mathrm{p}} \tag{30}$$

$\tau_\mathrm{L}$ is the time constant of the first-order system, and represents the time it takes for the laser output wavenumber to respond to a step change in $q$. $B$ represents the magnitude of wavenumber rate of change per unit $q$.

The general solution of Eq. 28 is:

$$\nu_\mathrm{rel}(t) = \exp\left(-\frac{t}{\tau_\mathrm{L}}\right)\left[-B\int_{t_1}^{t} \exp\left(\frac{s}{\tau_\mathrm{L}}\right) q(s)ds + \nu_\mathrm{rel}(t_1)\exp\left(\frac{t_1}{\tau_\mathrm{L}}\right)\right] \tag{31}$$

Here, $t_1$ [s] is an arbitrary starting time. In the following sections, we will solve Eq. 28 for various cases of current modulation.

### *A.1 Static tuning*

In the case of static tuning, the injection current is a fixed value $i_\mathrm{st}$, yielding a fixed value for $q = q_\mathrm{st} = i_\mathrm{st}^2 - i_0^2$. Additionally, $d\nu/dt = 0$, which yields the following simplified form of Eq. 28:

$$\nu_\mathrm{rel,st} = -B\tau_\mathrm{L}(i_\mathrm{st}^2 - i_0^2) \tag{32}$$

As mentioned in the previous section, during static tuning, the laser heat sink may change temperature due to the long timescales involved. However, this relation is informative as it indicates the locally nonlinear relationship between current and wavenumber modulation.

### *A.2 Sinusoidal heating modulation*

Before investigating the more complicated case of sinusoidal current modulation, the idealized case of sinusoidal variation in the laser heating $q(t)$ with scan rate $f$ [Hz] (period $\tau$ [s]) is investigated, where:

$$q(t) = q_\mathrm{A} \sin(2\pi f t) \tag{33}$$

The steady-state solution for Eq. 28 is:

$$\nu_\mathrm{rel}(t) = q_\mathrm{A} H_q \sin(2\pi f t - \phi_q) \tag{34}$$

$$H_q \equiv \frac{|v_\mathrm{pp}|}{|q_\mathrm{pp}|} = \frac{B\tau_\mathrm{L}}{\sqrt{(2\pi f \tau_\mathrm{L})^2 + 1}} \tag{35}$$

$$\phi_q \equiv \tan^{-1}(2\pi f \tau_\mathrm{L}) \tag{36}$$

A sample injection-current, effective heating, and chirp profile for an idealized 1 MHz sine wave is represented by the black curves in Fig. A.2. $H_q$ [$\mathrm{cm^{-1}A^{-2}}$] is the transfer function between the effective laser heating $q$ and the wavenumber modulation of the laser which is the ratio of the wavenumber amplitude and the effective heating amplitude $q_\mathrm{A}$. The scan depth of the laser under sinusoidal heating modulation is directly proportional to the product of the transfer function and the heating amplitude of the laser. This implies that the difference of the squares of the maximum and minimum injection current, $i_\mathrm{max}^2 - i_\mathrm{min}^2$, drives the scan depth, not necessarily the linear current amplitude. As such, with the same current amplitude, current modulation at a higher mean current will result in higher scan depth than current modulation at a lower mean current. At scan rates much higher than the natural frequency of the laser ($1/\tau_\mathrm{L}$), the transfer function simplifies to:

$$H_q \approx \frac{B}{2\pi f} \tag{37}$$

This indicates that at high modulation rates, $H_q \to 0$ which reflects the decrease in spectral scan depth at high scan rates. At very low scan frequencies relative to the laser natural frequency, $H_q$ is maximized at $B\tau_\mathrm{L}$.

$\phi_q$ [rad] is the phase lag of the wavenumber modulation relative to the effective laser heating. As the scan-rate $f$ becomes much larger than the natural frequency of the laser system ($1/\tau_\mathrm{L}$), $\phi_q \to 90°$, which is experimentally observed as the increasing phase lag between current and wavelength modulation at high scan rates, as seen in Fig. 2. On the other hand, at low scan rates, $\phi_q \to 0°$ which implies near zero phase lag for slow modulation. The transfer function and phase lag versus scan rate are plotted in Fig. 14 for $\tau_\mathrm{L} = 240$ ns. This value, specific to the primary laser used in this work, is determined in Section A.4. At $f = 1$ MHz, this time constant predicts a phase lag of approximately 56° and a transfer function that is ∼55% of its maximum low-frequency value.

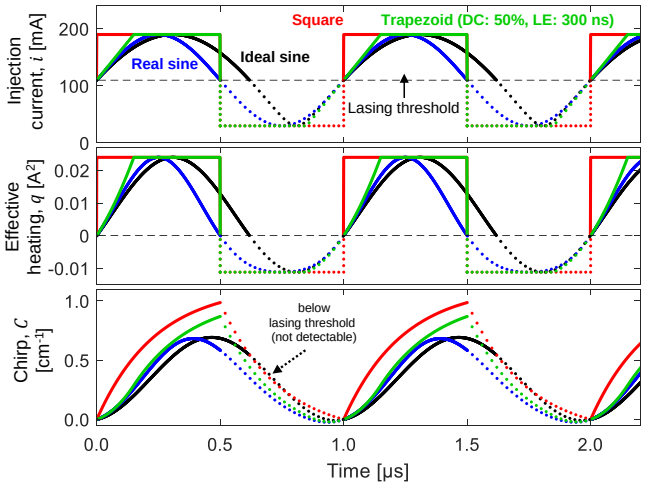


**Fig. 13** Sample simulated injection current profiles (*Top*), effective heating profiles (*Middle*), and chirp profiles (*Bottom*) for an ideal sinusoidal heating (black), sinusoidal injection current (blue), square-wave modulation at 50% duty cycle (red), and trapezoid-wave modulation with 50% duty cycle and $L = 0.3$ (green). The values of $B$ and $\tau_{\mathrm{L}}$ are the same for each type of modulation, and are equal to the the values found for the main laser studied in this work. The values of $i_{\mathrm{max}}$, $i_{\mathrm{min}}$, and $i_{\mathrm{th}}$ are set to 190, 30, and 110 mA respectively. The portion of the scans for which the laser is below the lasing threshold are indicated by the dotted portion of the curves. All chirp profiles are zeroed to the beginning of the upscan above the lasing threshold.

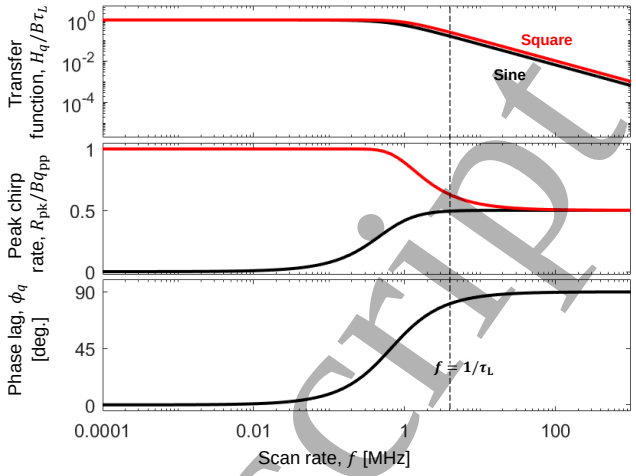


**Fig. 14** *Top*: The normalized transfer function for a square wave at 50% duty cycle (red) and ideal sine wave (black) *versus* scan rate $f$. *Middle*: Normalized peak upscan chirp rate *versus* scan rate for the aforementioned sine and square wave. *Bottom*: The phase lag for an ideal sine wave *versus* scan rate. $\tau_{\mathrm{L}}$ is set to 240 ns, the value found for the primary laser used in this work.

The transfer function is linear with $B$, implying that spectral scan depth is directly proportional to the thermal expansion coefficient of the DFB grating, $\alpha_{\mathrm{ex}}$, and the electrical resistance of the laser, $\rho$. Additionally, the transfer function and scan depth would be higher at higher wavenumbers (shorter wavelengths). The transfer function can also be increased by increasing the time constant of the laser $\tau_{\mathrm{L}}$. This can be achieved by either reducing the heat transfer coefficient between the laser and heat sink, $h$, or by increasing the overall heat capacity of the laser chip, $m_{\mathrm{L}}c_{\mathrm{p}}$ [J·K$^{-1}$], although this reduces $B$ and would likely result in an overall reduction in the transfer function. The transfer function plateaus to the value predicted by Eq. 37 for extremely large values of $\tau_{\mathrm{L}}$, implying diminishing returns for this strategy of transfer function enhancement. Increasing $\tau_{\mathrm{L}}$ can also have potential deleterious effects on the temperature stability of the laser over long time scales, so this is a non-ideal method to improve tuning characteristics.

### *A.3 Sinusoidal current modulation*

For a sinusoidal modulation of current with scan-rate $f$, current amplitude $i_{\mathrm{A}}$, and midrange current $i_{\mathrm{mid}} = i_0$ (the choice of reference condition 0 is arbitrary), the time-varying current and $q$ take the form:

$$i(t) = i_{\mathrm{A}} \sin(2\pi f t) + i_0 \tag{38}$$

$$q(t) = i_{\mathrm{A}}^2 \sin^2(2\pi f t) + 2 i_{\mathrm{A}} i_0 \sin(2\pi f t) \tag{39}$$

$$i_{\mathrm{A}} \equiv \frac{i_{\mathrm{max}} - i_{\mathrm{min}}}{2} \tag{40}$$

$$i_0 = i_{\mathrm{mid}} \tag{41}$$

To put the equation in terms of pure sinusoids, trigonometric double-angle identities are utilized:

$$q(t) = 2 i_{\mathrm{A}} i_{\mathrm{mid}} \sin(2\pi f t) - \frac{i_{\mathrm{A}}^2}{2} \sin(4\pi f t + \frac{\pi}{2}) + \frac{i_{\mathrm{A}}^2}{2} \tag{42}$$

The heating function $q(t)$ is now a sum of two sinusoids with frequency $2f$, $1f$, and $0f$ (DC component). The resulting solution to Eq. 28 will be a linear combination of the solutions for these individual sinusoidal forcing functions. These solutions can be obtained using Eqs. 34-36:

$$\nu_{\mathrm{rel}}(t) = -B q_{\mathrm{A}} \tau_{\mathrm{L}} \left[ \frac{\sin\left(2\pi f t - \tan^{-1}(2\pi f \tau_{\mathrm{L}})\right)}{\sqrt{(2\pi f \tau_{\mathrm{L}})^2 + 1}} + \frac{i_{\mathrm{A}}}{4 i_{\mathrm{mid}}} \frac{\sin\left(4\pi f t - \frac{\pi}{2} - \tan^{-1}(4\pi f \tau_{\mathrm{L}})\right)}{\sqrt{(4\pi f \tau_{\mathrm{L}})^2 + 1}} + \frac{i_{\mathrm{A}}}{4 i_{\mathrm{mid}}} \right] \tag{43}$$

This solution indicates that the wavenumber modulation is composed of two sine waves, one at the current-modulation frequency and another at a harmonic frequency twice that of the current-modulation. Additionally, there is an offset in the center wavenumber induced by the modulation, related to the fact that the mean current modulation is not equal to the mean value of the heating to the laser. This offset $\nu_{\mathrm{off}}$ is equal to:

$$\nu_{\mathrm{off}} = -\frac{i_{\mathrm{A}}}{4 i_{\mathrm{mid}}} \tau_{\mathrm{L}} B q_{\mathrm{A}} \tag{44}$$

A representative injection-current, effective heating, and chirp profile for 1 MHz sinusoidal injection current modulation are represented by the blue curves in Fig. A.2. Closed form equations for the transfer function and phase lag are not easily extracted from Eq. 43. Equation 43 is useful in that it reveals the functional form of the wavelength modulation due to sinusoidal current modulation. When fitting the relative wavenumber/chirp profile for a sinusoidal injection-current scan, it is thus more appropriate to fit the profile to a linear combination of a sine wave and another sine wave at double frequency, as has been performed in various works [8, 49]. This second harmonic has been noted in analysis of wavelength-modulation spectroscopy, where sinusoidal injection-current modulation is used and modeled [50].

Using Eq. 43, the ratio of the amplitude of the 2nd harmonic sinusoid and the sinusoid at the fundamental frequency is given by

$$\frac{\Delta\nu_{2f}}{\Delta\nu_{1f}} = \frac{i_\mathrm{A}}{4i_\mathrm{mid}} \frac{\sqrt{(2\pi f\tau_\mathrm{L})^2+1}}{\sqrt{(4\pi f\tau_\mathrm{L})^2+1}} \tag{45}$$

For low values of modulation frequency, this ratio approaches $i_\mathrm{A}/4i_\mathrm{mid}$, which can range from 0 to 25%, with lower values at lower current amplitudes. For high values of the modulation frequency, this ratio approaches half of the low-speed value: $i_\mathrm{A}/8i_\mathrm{mid}$, which ranges from 0 to 12.5%. Therefore, at high modulation frequencies and moderate values of current amplitude, the higher order sinusoid may be neglected to simplify the waveform analysis, and the solution for the wavenumber profile in Eq. 43 can simplify to the solution of pure sinusoidal heating in Eq. 34, albeit with a constant offset. As such, the trends of decreasing scan depth and increasing phase lag with modulation frequency established in Section A.2 are still applicable to the case of sinusoidal current modulation.

In the following paragraph, we detail how to calculate the spectral scan depth for sine-wave modulation. If the laser is scanned below lasing threshold, $i_\mathrm{th}$, the spectral scan depth can be found by finding the time $\tau_\mathrm{th}$ at which the $i(t) = i_\mathrm{th}$ and computing $\nu_\mathrm{rel}$ at this time. This time can be calculated as follows:

$$\tau_\mathrm{th} = \frac{1}{2\pi f}\sin^{-1}\left(\frac{i_\mathrm{th}-i_\mathrm{mid}}{i_\mathrm{A}}\right) \tag{46}$$

Next, the minimum value of $\nu_\mathrm{rel}$ must be found. Neglecting the first harmonic term (as discussed previously), this minimum occurs at the upscan "turnaround", $\tau_\mathrm{turn,up}$:

$$\tau_\mathrm{turn,up} \approx \frac{1}{2\pi f}\left(\tan^{-1}\left(2\pi f\tau_\mathrm{L}\right)+\frac{\pi}{2}\right) \tag{47}$$

The difference between these two values is the scan depth of the sinusoidal waveform:

$$\Delta\nu_\mathrm{sine} = \nu_\mathrm{rel}(\tau_\mathrm{th}) - \nu_\mathrm{rel}(\tau_\mathrm{turn,up}) \tag{48}$$

If the laser is not being scanned below the lasing threshold, then the maximum value of the wavenumber profile must be found and subtracted by the minimum wavenumber value from Eq. 47. If the second harmonic is neglected, then $\Delta\nu_\mathrm{sine}$ simplifies to the following form equivalent to the form for pure sinusoidal heating (see also Eq. 34):

$$\Delta\nu_\mathrm{sine} \approx \frac{\tau_\mathrm{L}Bq_\mathrm{A}}{\sqrt{(2\pi f\tau_\mathrm{L})^2+1}} \tag{49}$$

To find the chirp rate of the sinusoidal waveform, the absolute value of the time-derivative of Eq. 43 must be taken. If the higher harmonic is neglected, the chirp rate during the upscan is given by:

$$R_\mathrm{up}(t) = \frac{2\pi f\tau_\mathrm{L}Bq_\mathrm{A}}{\sqrt{(2\pi f\tau_\mathrm{L})^2+1}}\cos\left(2\pi fx - \tan^{-1}(2\pi f\tau_\mathrm{L})\right) \tag{50}$$

The peak chirp rate can be found by taking the time-derivative of the chirp rate and finding the times when this derivative equals zero. The peak chirp rate can be found by evaluating the chirp rate at these times. Still neglecting the higher harmonic, the peak chirp rate during the upscan is given by:

$$R_\mathrm{up,peak}(t) = \frac{2\pi f\tau_\mathrm{L}Bq_\mathrm{A}}{\sqrt{(2\pi f\tau_\mathrm{L})^2+1}} \tag{51}$$

The peak chirp rate is plotted against scan rate in the middle row of Fig. 14. The peak chirp rate increases as a function of the scan rate, but asymptotically approaches a maximum value of $Bq_\mathrm{A}$ for high modulation frequencies and can be approximated by $2\pi f\tau_\mathrm{L}Bq_\mathrm{A}$ for low modulation frequencies.

### *A.4 Square wave modulation*

For the case of square wave modulation at scan rate $f$ (period $\tau$) with duty cycle DC, the current and effective heating can be written as piecewise constant functions:

$$i(t) = \begin{cases} i_\mathrm{max} & \text{if } 0 \le t \le \mathrm{DC}\times\tau \\ i_\mathrm{min} & \text{if } \mathrm{DC}\times\tau < t \le \tau \end{cases} \tag{52}$$

$$q(t) = \begin{cases} q_\mathrm{max} & \text{if } 0 \le t \le \mathrm{DC}\times\tau \\ q_\mathrm{min} & \text{if } \mathrm{DC}\times\tau < t \le \tau \end{cases} \tag{53}$$

$$q_\mathrm{max} = i_\mathrm{max}^2 - i_0^2 \tag{54}$$

$$q_\mathrm{min} = i_\mathrm{min}^2 - i_0^2 \tag{55}$$

Equation 28 can be solved for these two periods yielding piecewise exponential solutions for the wavenumber profile:

$$\nu_\mathrm{rel}(t) = \begin{cases} -B\tau_\mathrm{L}q_\mathrm{max} + \left(\nu_\mathrm{rel}^\mathrm{max} + B\tau_\mathrm{L}q_\mathrm{max}\right)\exp\left(-\frac{t}{\tau_\mathrm{L}}\right) \\ \qquad\qquad \text{if } 0 \le t \le \mathrm{DC}\times\tau \\ -B\tau_\mathrm{L}q_\mathrm{min} + \left(\nu_\mathrm{rel}^\mathrm{min} + B\tau_\mathrm{L}q_\mathrm{min}\right)\exp\left(-\frac{t-\mathrm{DC}\tau}{\tau_\mathrm{L}}\right) \\ \qquad\qquad \text{if } \mathrm{DC}\times\tau < t \le \tau \end{cases} \tag{56}$$

Here, $\nu_{\text{rel}}^{\max}$ and $\nu_{\text{rel}}^{\min}$ are the maximum and minimum values of the wavenumber profile, achieved at beginning of the upscan and downscan respectively. By enforcing the continuity of $\nu_{\text{rel}}(t)$ at $t = \text{DC}\times\tau$ and the periodicity of the function ($\nu_{\text{rel}}(0) = \nu_{\text{rel}}(\tau)$), $\nu_{\text{rel}}^{\max}$ and $\nu_{\text{rel}}^{\min}$ can be solved for:

$$\nu_{\text{rel}}^{\max} = -B\tau_{\text{L}}\left[2q_{\text{A}}\frac{\exp\left(\text{DC}\frac{\tau}{\tau_{\text{L}}}\right)-1}{\exp\left(\frac{\tau}{\tau_{\text{L}}}\right)-1}+q_{\min}\right] \quad (57)$$

$$\nu_{\text{rel}}^{\min} = B\tau_{\text{L}}\left[2q_{\text{A}}\frac{\exp\left((1-\text{DC})\frac{\tau}{\tau_{\text{L}}}\right)-1}{\exp\left(\frac{\tau}{\tau_{\text{L}}}\right)-1}-q_{\max}\right] \quad (58)$$

The absolute value of these parameters are somewhat arbitrary, as they are relative to the arbitrary reference wavenumber $\nu_0$. The difference between the two however, is interesting, as this is the spectral scan depth achievable for the square wave:

$$\Delta\nu_{\text{square}} = \nu_{\text{rel}}^{\max} - \nu_{\text{rel}}^{\min} = 2\tau_{\text{L}}Bq_{\text{A}}\left[\coth\left(\frac{\tau}{2\tau_{\text{L}}}\right)-\frac{\cosh\left(\frac{\tau}{\tau_{\text{L}}}(\text{DC}-\frac{1}{2})\right)}{\sinh\left(\frac{\tau}{2\tau_{\text{L}}}\right)}\right] \quad (59)$$

This relation indicates that the spectral scan depth for square-wave modulation is linearly proportional to the amplitude of laser heating $q_{\text{A}}$. The term in the fraction encodes the dependence of the scan depth on the modulation period $\tau$ and the duty cycle DC. By taking the derivative of Eq. 59 with respect to the duty cycle, it can be shown that the maximum value of the scan depth is achieved at a duty cycle of 50%, which matches with the experimental observations from Section 3.1. If Eq. 59 is evaluated for a duty cycle of 50%, the maximum scan depth for a given scan frequency can be found:

$$\Delta\nu_{\text{square}}^{\text{opt}} = 2\tau_{\text{L}}Bq_{\text{A}}\left[\coth\left(\frac{\tau}{2\tau_{\text{L}}}\right)-\text{csch}\left(\frac{\tau}{2\tau_{\text{L}}}\right)\right] \quad (60)$$

For square-wave modulation at 50% duty-cycle, the transfer function between spectral scan depth and peak-to-peak laser heating can be written as:

$$H_{q,\text{square}}^{\text{opt}} = B\tau_{\text{L}}\left[\coth\left(\frac{\tau}{2\tau_{\text{L}}}\right)-\text{csch}\left(\frac{\tau}{2\tau_{\text{L}}}\right)\right] \quad (61)$$

At scan rates much greater than the natural frequency of the laser ($1/\tau_{\text{L}}$), this transfer function simplifies to:

$$H_{q,\text{square}}^{\text{opt}} \approx \frac{B}{4f} \quad (62)$$

This function is generally greater than the transfer function for sinusoidal modulation (Eq. 37) by a factor of $\pi/2$ (+57%), which is supported by the experimental observation that spectral scan-depth is improved for square-wave modulation over sinusoidal modulation. At these high speeds, for duty cycles not equal to 50%, a factor of $4\text{DC}(1-\text{DC})$ must be multiplied to the transfer function to account for the reduction in scan depth. At scan rates much lower than the natural frequency of the laser, the transfer function approaches $B\tau_{\text{L}}$, which is the same value for pure sinusoidal modulation, implying reduced tuning benefits for square wave modulation for low-speed scanning. This low-speed approximation for the transfer function is relatively insensitive to duty cycle, except at extreme values ($\text{DC} < 2f\tau_{\text{L}}$ or $\text{DC} > 1-2f\tau_{\text{L}}$), where the tuning performance drastically drops to near 0. Across all scan frequencies, the scan depth of a square wave is approximately equal to that of a sine wave at duty cycles near 20 or 80%.

The laser parameters for the QCL used in Sections 2–3.4.1 were determined using the relations developed above for square-wave modulation. $\tau_{\text{L}}$ was found by fitting the chirp profile for the extended square wave from Fig. 7 with an exponential function in the form provided by Eq. 56. $\tau_{\text{L}}$ was determined to be approximately 240 ns. Next, the square-wave transfer function $H_{q,\text{square}}$ at 1 MHz and 50% duty cycle was determined by observing the increase in spectral scan depth as the heating amplitude $q_{\text{A}}$ was increased (by increasing the fractional current $F$ from 42% to 84%). A linear function was fitted to the plot of scan depth versus heating amplitude and the slope of the resulting line was used to find the approximate value of the transfer function of $H_{q,\text{square}}^{\text{opt}} \sim 2.8\cdot10^{-5}$ cm$^{-1}\cdot$(mA)$^{-2}$. Eq. 61 was then solved for $B$ and evaluated with knowledge of $\tau_{\text{L}}$, $f$, and $H_{q,\text{square}}^{\text{opt}}\cdot$ $B$ was found to have an approximate value of $B \sim 1.5\cdot10^{-4}$ cm$^{-1}$/(mA$^2\cdot$µs). A representative injection-current, effective heating, and chirp profile for 1 MHz square-wave at 50% duty cycle are represented by the red curves in Fig. A.2, using the aforementioned laser parameters. The transfer functions versus scan rate for an ideal sine wave (as discussed in Section A.2 and 50% duty cycle square wave are compared in Fig. 14 along with the phase lag, $\phi_q$ for an ideal sine wave.

The chirp rate for square-wave modulation may be found by taking the absolute value of the derivative of Eq. 56 with respect to time. The peak chirp rate $R_{\text{peak}}$ during the upscan can be found by taking the value of the chirp rate at time zero:

$$R_{\text{peak}} = 2Bq_{\text{A}}\frac{\exp\left(\frac{\tau}{\tau_{\text{L}}}\right)-\exp\left(\text{DC}\frac{\tau}{\tau_{\text{L}}}\right)}{\exp\left(\frac{\tau}{\tau_{\text{L}}}\right)-1} \quad (63)$$

The peak chirp rate increases linearly with the heating amplitude and $B$. Additionally, the peak chirp rate is maximized at a duty cycle of 0, and is minimized at a duty cycle of 1, which supports the experimental observation of improved usable scan depth at duty cycles higher than 50%, as seen in Section 3.3. The peak chirp rate for a square wave at 50% duty cycle is plotted against scan rate in the middle row if Fig. 14. In contrast with sinusoidal modulation, the $R_{\text{peak}}$ decreases with increasing modulation rate, as the temperature extremes

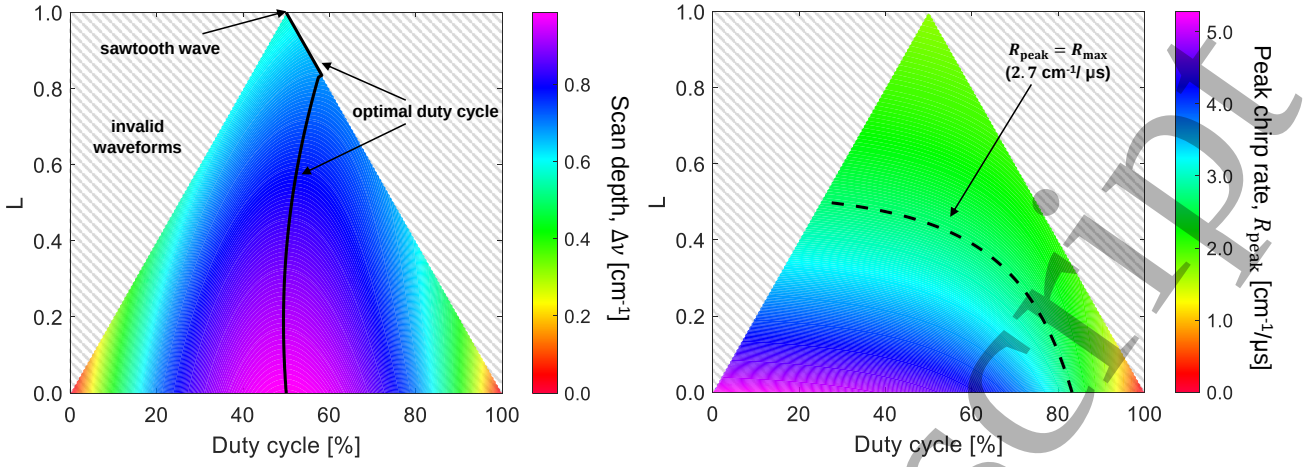


**Fig. 15** *Left*: Spectral scan depth *versus* duty cycle and $L$ for a simulated trapezoidal wave. *Right*: Peak upscan chirp rate *versus* duty cycle and $L$ for the same simulated trapezoidal wave. $B$, $\tau_L$, $i_{max}$, and $i_{min}$ are the same as in Figs. A.2 and 14.

of the laser become reduced, resulting in reduced heat transfer during the beginning of the upscan. At these high modulation rates, the peak chirp rate approaches $2(1-D)Bq_A$. For a 50% duty cycle, this value is equivalent to that for high-speed sinusoidal modulation. At low modulation rates, $R_{peak}$ approaches $2Bq_A$, with a weak dependence on duty cycle, except at duty cycles near 100% (DC$> 1-2f\tau_L$), where the peak chirp rate rapidly drops to zero.

### *A.5 Trapezoidal wave modulation*

For the case of trapezoid-wave modulation at scan rate $f$ (period $\tau$), duty cycle DC, and leading edge ramp time LE, the current and effective heating can be written as piecewise functions:

$$i(t) = \begin{cases} i_{max} & \text{if } 0 \le t \le (\text{DC} - \frac{L}{2})\tau \\ i_{min} & \text{if } (\text{DC} - \frac{L}{2})\tau < t \le (1-L)\tau \\ i_{ramp}(t) & \text{if } (1-L)\tau < t < \tau \end{cases} \quad (64)$$

$$q(t) = \begin{cases} q_{max} & \text{if } 0 \le t \le (\text{DC} - \frac{L}{2})\tau \\ q_{min} & \text{if } (\text{DC} - \frac{L}{2})\tau < t \le (1-L)\tau \\ q_{ramp}(t) & \text{if } (1-L)\tau < t < \tau \end{cases} \quad (65)$$

where

$$L = \frac{\text{LE}}{\tau} \quad (66)$$

$$i_{ramp}(t) = j(t-(1-L)\tau) + i_{min} \quad (67)$$

$$q_{ramp}(t) = i_{ramp}^2(t) - i_0^2 \quad (68)$$

$$j = \frac{i_{max} - i_{min}}{L\tau} \quad (69)$$

For a given duty cycle, $L$ (the fraction of the scan over which the ramp occurs) has a maximal value, above which the flat part of the upscan or downscan no longer exist:

$$L_{max} = \begin{cases} 2 \times \text{DC} & \text{if } \text{DC} \ge 1/2 \\ 2(1-\text{DC}) & \text{if } \text{DC} \le 1/2 \end{cases} \quad (70)$$

For a duty cycle of 50%, when $L = 1$, the waveform takes the form of a sawtooth wave.

Similar to the case of the square wave, the solution for $\nu_{rel}(t)$ may be found by solving Eq. 31 for the various phases of the trapezoid wave and ensuring continuity at $t = (\text{DC} - \frac{L}{2})\tau$ and $t = (1-L)\tau$, as well as ensuring the periodicity of the function $\nu_{rel}(0) = \nu_{rel}(\tau)$.

The resulting solution is cumbersome to write in its entirety here, but the solution may be numerically analyzed and compared to that for the pure square wave. A representative injection-current, effective heating, and chirp profile for 1 MHz trapezoid wave at 50% duty cycle with $L = 0.3$ are represented by the green curves in Fig. A.2. Unlike the pure square wave, the spectral scan depth must be found by considering the time at which the current rises above the lasing threshold during the ramp, $\tau_{th}$. If this point occurs before the downscan "turnaround", where $\nu_{rel}$ reaches a local maximum, which occurs at time $\tau_{turn,down}$ (when $d\nu_{ramp}/dt = 0$), then the spectral scan depth is the difference in $\nu_{rel}$ at the turnaround and the end of the upscan. If $\tau_{th} > \tau_{turn,down}$, then the spectral scan depth is the difference between $\nu_{rel}(\tau_{th})$ and $\nu_{rel}((\text{DC} - 1/2)\tau)$. If the current stays above the laser threshold during the entire scan period, then the spectral scan depth may be found by taking the difference between the maximum and minimum values of $\nu_{rel}$.

The spectral scan depth is mapped as a function of each combination of duty cycle and $L$ on the left side of Fig. 15 for a trapezoid wave at $f = 1$ MHz, $i_{min} = 30$ mA and $i_{max} = 190$ mA, using the laser parameters found above ($B = 1.5{\cdot}10^{-4}$ cm$^{-1}$/(mA$^2{\cdot}$µs), $\tau_L = 240$ ns), with the assumption that the lasing threshold is exceeded be-

fore the downscan turnaround (for simplicity). The scan depth is maximized at a duty cycle of 50% and when $L = 0$. As $L$ is increased, scan depth generally drops for a given value of duty cycle. This is true regardless of scan frequency, although the sensitivity of the scan depth to $L$ is reduced at lower modulation rates. The scan depth of a trapzedoidal waveform at 50% duty cycle is similar to that of a sine wave at values of $L$ between 70 and 80%. It is interesting to note that the duty cycle that maximizes spectral scan depth (plotted as a black curve on Fig. 15 is greater than 50% when $L \neq 0$, as observed experimentally in Fig. 4 in Section 3.3. This is because for a pure square wave, 50% duty cycle offers an even amount of cooling and heating of the laser system, as the time averaged value of $q$ is equal to the average between the maximum and minimum value of $q$. When a leading edge ramp is added to the injection-current waveform, the ramp in $q$ is quadratic, not linear, and as such, the average value of $q$ during the ramp is no longer equal to the average between the maximum and minimum values of $q$. The average value of $q$ ends up being lower than in the linear case, resulting in increased cooling duration compared to heating over a modulation period. To compensate for this, the duty cycle can be raised to increase the heating period to balance the duration of cooling and heating, to maximize the scan depth. Above a certain value of $L$ (in this case, $\sim$75%), the optimal duty cycle ends up being the maximum allowable value for the given value of $L$. This is reflected by the black curve on the left of Fig. 15 coinciding with the right boundary of the triangle of valid waveforms. For high values of $L$, this implies that the optimal waveform for maximimzing spectral scan depth is closer to a sawtooth waveform.

The peak chirp rate (durng the upscan) is also mapped as a function of duty cycle and $L$ on the right side of Fig. 15 for the same laser parameters mentioned above. It is interesting to note that the peak chirp rate typically occurs at the top of the leading edge ramp, at the start of the flat part of the upscan. As noted for pure square waves, the peak chirp rate increases with decreasing duty cycle for a given value of $L$. For 1 MHz modulation, as $L$ increases at a fixed duty cycle, the peak chirp rate decreases, which reflects the increasing "usefullness" of waveforms with longer leading edges when scanning narrow spectral features, as outlined in Section 3.3. The maximum allowable value for the chirp rate for narrow spectral detection ($\delta\nu_{\min} \sim 0.027$ cm$^{-1}$ for CO near 0.25 atm), $R_{\max} = 2.7$ cm$^{-1}$/µs is indicated by the black dashed line on the right side of Fig. 15. The region above and to the left of this black dashed line indicates waveforms that have limited usable scan depth when scanning features with narrow spectral widths. This trend of decreased peak chirp rates at higher values of $L$ and increased scan depths at duty cycles greater than 50% explain why the optimal waveforms found in Section 3.3 had values of $L$ that were 30–40% and duty cycles that were 60–70%.

## References


1. Goldenstein CS, Spearrin R, Jeffries JB, Hanson RK (2017) Infrared laser-absorption sensing for combustion gases. Progress in Energy and Combustion Science 60:132–176, DOI 10.1016/j.pecs.2016.12.002, URL https://linkinghub.elsevier.com/retrieve/pii/S0360128516300843
2. Lackner M, Totschnig G, Winter F, Ortsiefer M, Amann MC, Shau R, Rosskopf J (2003) Demonstration of methane spectroscopy using a vertical-cavity surface-emitting laser at 1.68 $\mu$m with up to 5 MHz repetition rate. Measurement Science and Technology 14(1):101–106, DOI 10.1088/0957-0233/14/1/315
3. MacDonald ME, Brandis AM, Cruden BA (2018) Temperature and CO Number Density Measurements in Shocked CO and CO2 via Tunable Diode Laser Absorption Spectroscopy. In: 2018 Joint Thermophysics and Heat Transfer Conference, American Institute of Aeronautics and Astronautics, Reston, Virginia, pp 1–23, DOI 10.2514/6.2018-4067, URL https://arc.aiaa.org/doi/10.2514/6.2018-4067
4. Kaebe BD, Robins NP, Boyson TK, Kleine H, O'Byrne S (2018) 16 MHz scanning rate direct absorption temperature measurements using a single vertical-cavity surface-emitting laser diode. Applied Optics 57(20):5680, DOI 10.1364/ao.57.005680
5. Raza M, Ma L, Yao C, Yang M, Wang Z, Wang Q, Kan R, Ren W (2020) MHz-rate scanned-wavelength direct absorption spectroscopy using a distributed feedback diode laser at 2.3 µm. Optics & Laser Technology 130(May):106344, DOI 10.1016/j.optlastec.2020.106344, URL https://linkinghub.elsevier.com/retrieve/pii/S0030399220309774
6. Mathews GC, Blaisdell MG, Lemcherfi AI, Slabaugh CD, Goldenstein CS (2021) High-bandwidth absorption-spectroscopy measurements of temperature, pressure, CO, and H 2 O in the annulus of a rotating detonation rocket engine. Applied Physics B: Lasers and Optics 127(12):1–23, DOI 10.1007/s00340-021-07703-9, URL https://doi.org/10.1007/s00340-021-07703-9
7. Nair AP, Lee DD, Pineda DI, Kriesel J, Hargus WA, Bennewitz JW, Danczyk SA, Spearrin RM (2020) MHz laser absorption spectroscopy via diplexed RF modulation for pressure, temperature, and species in rotating detonation rocket flows. Applied Physics B 126(8):138, DOI 10.1007/s00340-020-07483-8, URL https://link.springer.com/10.1007/s00340-020-07483-8
8. Jelloian CC, Bendana FA, Wei C, Spearrin RM, MacDonald ME (2022) Nonequilibrium Vibrational, Rotational, and Translational Thermometry via Megahertz Laser Absorption of CO. Journal of Thermophysics and Heat Transfer 36(2):266–275, DOI 10.2514/1.T6376, URL https://arc.aiaa.org/doi/10.2514/1.T6376
9. Mathews G, Goldenstein C (2020) Near-GHz scanned-wavelength-modulation spectroscopy for MHz thermometry and H 2 O measurements in aluminized fireballs of energetic materials. Applied Physics B: Lasers and Optics 126(11):1–17, DOI 10.1007/s00340-020-07527-z, URL https://doi.org/10.1007/s00340-020-07527-z
10. Sanders ST, Baldwin JA, Jenkins TP, Baer DS, Hanson RK (2000) Diode-laser sensor for monitoring multi-

ple combustion parameters in pulse detonation engines. Proceedings of the Combustion Institute 28(1):587–594, DOI 10.1016/s0082-0784(00)80258-1

11. Ma L, Sanders ST, Jeffries JB, Hanson RK (2002) Monitoring and control of a pulse detonation engine using a diode-laser fuel concentration and temperature sensor. Proceedings of the Combustion Institute 29(1):161–166, DOI 10.1016/S1540-7489(02)80025-6
12. Klingbeil AE, Jeffries JB, Hanson RK (2007) Design of a fiber-coupled mid-infrared fuel sensor for pulse detonation engines. AIAA Journal 45(4):772–778, DOI 10.2514/1.26504
13. Li H, Farooq A, Jeffries JB, Hanson RK (2007) Near-infrared diode laser absorption sensor for rapid measurements of temperature and water vapor in a shock tube. Applied Physics B: Lasers and Optics 89(2-3):407–416, DOI 10.1007/s00340-007-2781-9
14. Alturaifi SA, Mathieu O, Petersen EL (2022) An experimental and modeling study of ammonia pyrolysis. Combustion and Flame 235:111694, DOI 10.1016/j.combustflame.2021.111694, URL https://linkinghub.elsevier.com/retrieve/pii/S0010218021004375
15. Goldenstein CS, Spearrin RM, Jeffries JB, Hanson RK (2016) Infrared laser absorption sensing for combustion flows. Progress in Energy and Combustion Science
16. Arroyo Instruments (2015) 6300 Series ComboSource User's Manual. URL https://www.arroyoinstruments.com/product-lines/6300
17. Nair AP, Jelloian C, Morrow DS, Bendana FA, Pineda DI, Spearrin RM (2020) MHz mid-infrared laser absorption sensor for carbon monoxide and temperature behind detonation waves. In: AIAA Scitech 2020 Forum, American Institute of Aeronautics and Astronautics, Reston, Virginia, DOI 10.2514/6.2020-0733, URL https://arc.aiaa.org/doi/10.2514/6.2020-0733
18. Nair AP, Lee DD, Pineda DI, Kriesel J, Hargus WA, Bennewitz JW, Bigler B, Danczyk SA, Spearrin RM (2021) Methane-Oxygen Rotating Detonation Exhaust Thermodynamics with Variable Mixing, Equivalence Ratio, and Mass Flux. Aerospace Science and Technology 113:106683, DOI 10.1016/j.ast.2021.106683
19. Zeller W, Naehle L, Fuchs P, Gerschuetz F, Hildebrandt L, Koeth J (2010) DFB lasers between 760 nm and 16 $\mu$m for sensing applications. Sensors 10(4):2492–2510, DOI 10.3390/s100402492
20. Tombez L, Schilt S, Di Francesco J, Führer T, Rein B, Walther T, Di Domenico G, Hofstetter D, Thomann P (2012) Linewidth of a quantum-cascade laser assessed from its frequency noise spectrum and impact of the current driver. Applied Physics B: Lasers and Optics 109(3):407–414, DOI 10.1007/s00340-012-5005-x
21. Yulianto N, Widiyatmoko B, Priambodo PS (2015) Temperature Effect towards DFB Laser Wavelength on Microwave Generation Based on Two Optical Wave Mixing. International Journal of Optoelectronic Engineering 5(2):21–27, DOI 10.5923/j.ijoe.20150502.01
22. Spearrin RM, Goldenstein CS, Schultz IA, Jeffries JB, Hanson RK (2014) Simultaneous sensing of temperature, CO, and CO2 in a scramjet combustor using quantum cascade laser absorption spectroscopy. Applied Physics B: Lasers and Optics 117(2):689–698, DOI 10.1007/s00340-014-5884-0
23. Lee DD, Bendana FA, Schumaker SA, Spearrin RM (2018) Wavelength modulation spectroscopy near 5 $\mu$m for carbon monoxide sensing in a high-pressure kerosene-fueled liquid rocket combustor. Applied Physics B 124(5):77, DOI 10.1007/s00340-018-6945-6
24. Pineda DI, Bendana FA, Schwarm KK, Spearrin RM (2019) Multi-isotopologue laser absorption spectroscopy of carbon monoxide for high-temperature chemical kinetic studies of fuel mixtures. Combustion and Flame 207:379–390, DOI 10.1016/j.combustflame.2019.05.030, URL https://linkinghub.elsevier.com/retrieve/pii/S0010218019302433
25. Normand E, McCulloch M, Duxbury G, Langford N (2003) Fast, real-time spectrometer based on a pulsed quantum-cascade laser. Optics Letters 28(1):16, DOI 10.1364/ol.28.000016
26. Wysocki G, McCurdy M, So S, Weidmann D, Roller C, Curl RF, Tittel FK (2004) Pulsed quantum-cascade laser-based sensor for trace-gas detection of carbonyl sulfide. Applied Optics 43(32):6040–6046, DOI 10.1364/AO.43.006040
27. Van Helden JH, Horrocks SJ, Ritchie GA (2008) Application of quantum cascade lasers in studies of low-pressure plasmas: Characterization of rapid passage effects on density and temperature measurements. Applied Physics Letters 92(8):1–4, DOI 10.1063/1.2885725
28. Northern JH, Ritchie GAD, Smakman EP, van Helden JH, Cockburn J, Duxbury G (2010) Rapid passage signals induced by chirped quantum cascade laser radiation: K state dependent-delay effects in the $\nu$_2 band of NH_3. Optics Letters 35(16):2750, DOI 10.1364/ol.35.002750
29. Nwaboh JA, Werhahn O, Schiel D (2011) Measurement of CO amount fractions using a pulsed quantum-cascade laser operated in the intrapulse mode. Applied Physics B: Lasers and Optics 103(4):947–957, DOI 10.1007/s00340-010-4322-1
30. Chrystie RS, Nasir EF, Farooq A (2014) Calibration-free and ultra-fast sensing of temperature and species in the intrapulse mode. Optics InfoBase Conference Papers 39(23):6620–6623, DOI 10.1364/lacsea.2014.lw4b.7
31. Chrystie RS, Nasir EF, Farooq A (2015) Towards simultaneous calibration-free and ultra-fast sensing of temperature and species in the intrapulse mode. Proceedings of the Combustion Institute 35(3):3757–3764, DOI 10.1016/j.proci.2014.06.069, URL http://dx.doi.org/10.1016/j.proci.2014.06.069https://linkinghub.elsevier.com/retrieve/pii/S1540748914002272
32. Nasir EF, Farooq A (2018) Intra-pulse laser absorption sensor with cavity enhancement for oxidation experiments in a rapid compression machine. Optics Express 26(11):14601, DOI 10.1364/oe.26.014601
33. McCulloch MT, Normand EL, Langford N, Duxbury G, Newnham DA (2003) Highly sensitive detection of trace gases using the time-resolved frequency downchirp from pulsed quantum-cascade lasers. Journal of the Optical Society of America B 20(8):1761, DOI 10.1364/josab.20.001761
34. Hanson RK, Spearrin RM, Goldenstein CS (2016) Spectroscopy and Optical Diagnostics for Gases. Springer International Publishing, Cham, DOI 10.1007/978-3-319-23252-2

35. Schwarm KK, Wei C, Pineda DI, Mitchell Spearrin R, Spearrin RM (2019) Time-resolved laser absorption imaging of ethane at 2 kHz in unsteady partially premixed flames. Applied Optics 58(21):5656, DOI 10.1364/AO.58.005656, URL https://www.osapublishing.org/abstract.cfm?URI=ao-58-21-5656
36. Olivero J, Longbothum R (1977) Empirical fits to the Voigt line width: A brief review. Journal of Quantitative Spectroscopy and Radiative Transfer 17(2):233–236, DOI 10.1016/0022-4073(77)90161-3
37. Gordon I, Rothman L, Hargreaves R, Hashemi R, Karlovets E, Skinner F, Conway E, Hill C, Kochanov R, Tan Y, Wcisło P, Finenko A, Nelson K, Bernath P, Birk M, Boudon V, Campargue A, Chance K, Coustenis A, Drouin B, Flaud J, Gamache R, Hodges J, Jacquemart D, Mlawer E, Nikitin A, Perevalov V, Rotger M, Tennyson J, Toon G, Tran H, Tyuterev V, Adkins E, Baker A, Barbe A, Canè E, Császár A, Dudaryonok A, Egorov O, Fleisher A, Fleurbaey H, Foltynowicz A, Furtenbacher T, Harrison J, Hartmann J, Horneman V, Huang X, Karman T, Karns J, Kassi S, Kleiner I, Kofman V, Kwabia–Tchana F, Lavrentieva N, Lee T, Long D, Lukashevskaya A, Lyulin O, Makhnev V, Matt W, Massie S, Melosso M, Mikhailenko S, Mondelain D, Müller H, Naumenko O, Perrin A, Polyansky O, Raddaoui E, Raston P, Reed Z, Rey M, Richard C, Tóbiás R, Sadiek I, Schwenke D, Starikova E, Sung K, Tamassia F, Tashkun S, Vander Auwera J, Vasilenko I, Vigasin A, Villanueva G, Vispoel B, Wagner G, Yachmenev A, Yurchenko S (2022) The HITRAN2020 molecular spectroscopic database. Journal of Quantitative Spectroscopy and Radiative Transfer 277:107949, DOI 10.1016/j.jqsrt.2021.107949
38. McLean A, Mitchell C, Swanston D (1994) Implementation of an efficient analytical approximation to the Voigt function for photoemission lineshape analysis. Journal of Electron Spectroscopy and Related Phenomena 69(2):125–132, DOI 10.1016/0368-2048(94)02189-7
39. Ohtsubo J (1977) Semiconductor lasers and theory. Academic Press, DOI 10.1007/978-3-319-56138-7{_}3
40. Jin X, Chuang SL (1985) High-speed modulation of semiconductor lasers. IEEI Transactions on Electron Devices 32(12):2572–2584, DOI 10.1364/ofc.1984.mj1
41. Browne S, Ziegler J, Shepherd JE (2004) Numerical Solution Methods for Shock and Detonation Jump Conditions. GALCIT Report FM2006006
42. Goodwin DG, Moffat HK, Speth RL (2018) Cantera: An object-oriented software toolkit for chemical kinetics, thermodynamics, and transport processes. DOI 10.5281/zenodo.170284
43. Smith GP, Golden DM, Frenklach M, Moriarty NW, Eiteneer B, Goldenberg M, Bowman CT, Hanson RK, Song S, Gardiner WC, Lissianski VV, Qin Z (1999) GRI-MECH 3.0. URL http://combustion.berkeley.edu/gri-mech/version30/text30.html
44. Taylor G (1950) The dynamics of the combustion products behind plane and spherical detonation fronts in explosives. Proceedings of the Royal Society of London Series A Mathematical and Physical Sciences 200(1061):235–247, DOI 10.1098/rspa.1950.0014
45. Bendana FA, Lee DD, Wei C, Pineda DI, Spearrin RM (2019) Line mixing and broadening in the v(1→3) first overtone bandhead of carbon monoxide at high temperatures and high pressures. Journal of Quantitative Spectroscopy and Radiative Transfer 239:106636, DOI 10.1016/j.jqsrt.2019.106636, URL https://linkinghub.elsevier.com/retrieve/pii/S0022407319304042
46. Bendana FA (2020) Shock tube kinetics and laser absorption diagnostics for liquid- and hybrid- propellant rocket combustion analysis. PhD thesis, University of California, Los Angeles
47. Anderson JD (2002) Modern Compressible Flow, 3rd edn. McGraw-Hill
48. Campbell MF, Owen KG, Davidson DF, Hanson RK (2017) Dependence of Calculated Postshock Thermodynamic Variables on Vibrational Equilibrium and Input Uncertainty. Journal of Thermophysics and Heat Transfer 31(3):586–608, DOI 10.2514/1.T4952
49. Jelloian C, Minesi NQ, Spearrin RM (2022) High-speed interband cascade laser absorption sensor for multiple temperatures in CO2 rovibrational non-equilibrium. In: AIAA SCITECH 2022 Forum, American Institute of Aeronautics and Astronautics, Reston, Virginia, pp 2022–2398, DOI 10.2514/6.2022-2398, URL https://arc.aiaa.org/doi/10.2514/6.2022-2398
50. Strand CL (2014) Scanned Wavelength-Modulation Absorption Spectroscopy with Application to Hypersonic Impulse Flow Facilities. PhD thesis, Stanford University